Terr. Atmos. Ocean. Sci., Vol. 30, No. 2, 185-214, April 2019

doi: 10.3319/TAO.2018.12.16.01

The roles of vertical wind shear and topography in formation of convective asymmetries in Typhoon Nanmadol (2011)

Kun-Hsuan Chou [*], Chun-Ming Yeh, and Shu-Jeng Lin

Department of Atmospheric Sciences, Chinese Culture University, Taipei City, Taiwan

Article history:

Received 7 May 2018
Revised 22 November 2018
Accepted 16 December 2018

Keywords:

Vertical wind shear, Convection asymmetry, Asymmetric secondary circulation

Citation:

Chou, K.-H., C.-M. Yeh, and S.-J. Lin, 2019: The roles of vertical wind shear and topography in formation of convective asymmetries in Typhoon Nanmadol (2011). Terr. Atmos. Ocean. Sci., 30, 185-214, doi: 10.3319/TAO.2018.12.16.01

ABSTRACT

The effects of terrain and environmental vertical wind shear on the intensity, structure, and asymmetric convection of Typhoon Nanmadol (2011) were investigated using a high-resolution numerical model. Terrain-removed sensitivity experiments were conducted to elucidate the relative role of terrain in the formation of the storm's asymmetric convection. Several sensitivity experiments were also employed to examine whether convective asymmetry formed in the simulated storm was influenced by model physics or existence of Typhoon Talas (2011). The control experiment shows that the simulations of the overall track and intensity evolution and asymmetric convection of Nanmadol were reasonably close to observations. Storm-relative composited analyses prove that environmental vertical wind shear enhances the storm's secondary circulation (low-level inflow, upward motion, and upper-level outflow) over the downshear side, but suppresses secondary circulation over the upshear side, thus inducing asymmetric secondary circulation within the storm, the dynamical pattern of which can be explained by the superposition effect of environmental vertical wind shear. The results of sensitivity experiments indicate that the underlying terrain, the model physics, and the circulation of the Talas didn't exert any obvious influence on the asymmetric convection and secondary circulation of the simulated storm. Therefore, the results presented here not only indicate that environmental vertical wind shear played a dominant role in forming the asymmetric convective pattern of Nanmadol, but also demonstrate that the proposed shear-induced dynamic pattern of the asymmetric secondary circulation is robust.

1. INTRODUCTION

In recent years, three typhoons with obvious convective asymmetry have struck Taiwan, namely Mindulle (2004), Fanapi (2010), and Nanmadol (2011). Each of these typhoons not only induced strong precipitation at the inner core of the storm but also caused a proportionally larger amount of cumulative rainfall on the active convection side. As these typhoons appear to have been influenced by the topography of the Philippines or Taiwan, the occurrence of convective asymmetry could be related to terrain effects. It is necessary to understand whether topography plays a role in forming asymmetric convection in tropical cyclones (TCs).

In 2011, Typhoon Nanmadol was the strongest tropical cyclone that made landfall in the Philippines and was also the first cyclone of the year to directly impact both Taiwan and China. According to the Joint Typhoon Warning Center (JTWC) Best Track data, Nanmadol originally developed from an area of low pressure that had formed to the east of the Philippines on 19 August. It then moved northwards and evolved as follows: at 1200 UTC on 22 August it became a tropical depression, at 1200 UTC on 23 August it became a tropical storm, at 1800 UTC on 24 August it evolved into a typhoon, and it then reached its peak strength with 1-min sustained winds of 140 knots at 0600 UTC on 26 August. Nanmadol then continued to move northwestward, and at 0000 UTC on 27 August, it made landfall over the northeastern corner of the Philippines with sustained winds of 125 knots. Thereafter, it continued to weaken as it headed northwestward toward Taiwan, and during this period, its outer circulation began to affect Taiwan. The storm then

---

* *Corresponding author*
E-mail: zkx@faculty.pccu.edu.tw

interacted with the topography of Luzon Island, and Nanmadol made its second landfall over southeastern Taiwan with sustained winds of 65 knots, prior to rapidly weakening at around 0000 UTC on 29 August. A tremendous amount of precipitation occurred over southern Taiwan (up to 127 mm of hourly rainfall was observed over southern Taiwan at Hengchun station of the Central Weather Bureau) as interaction with land caused it to weaken severely. Six hours later, Nanmadol accelerated toward the northwest and entered the Taiwan Strait at around 0600 UTC on 29 August. It slowly accelerated toward China, and weakened to a tropical depression with sustained winds of 30 knots at 0000 UTC on 30 August. After making final landfall over China, Nanmadol then rapidly weakened and dissipated at 0000 UTC on 31 August.

Of considerable scientific interest is the long-duration and steady-state azimuthal wavenumber-1 asymmetric convection that formed as Typhoon Nanmadol passed the Philippines and Taiwan. Figure 1 shows satellite microwave images of the brightness temperature of Nanmadol during the relevant period. Strong convection began to develop in the southern part of the storm when it approached Luzon Island (Figs. 1a - c). Inner core convection eroded on the west side as it approached and passed the tip of Luzon, but there is

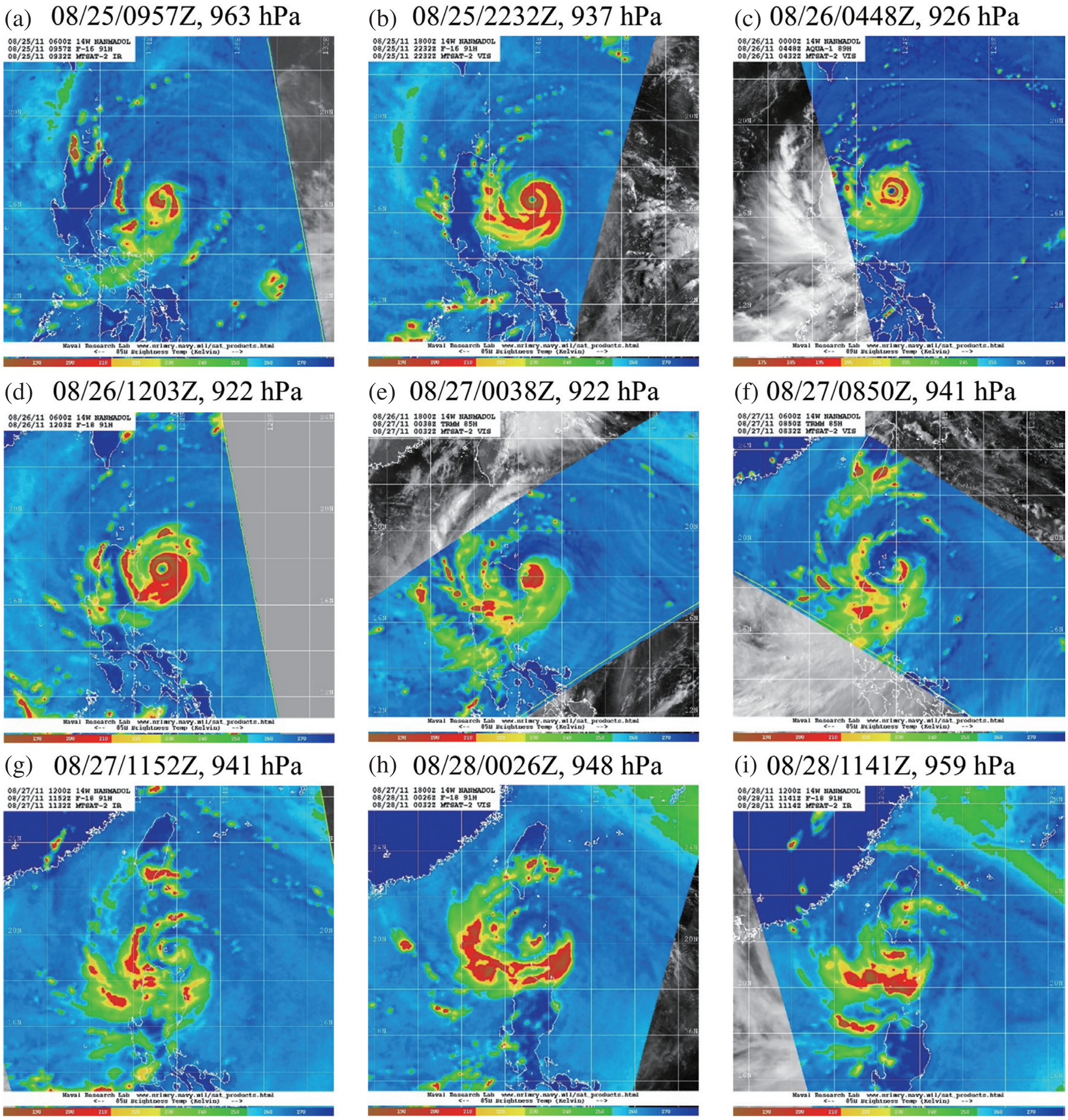
(a) 08/25/0957Z, 963 hPa
(b) 08/25/2232Z, 937 hPa
(c) 08/26/0448Z, 926 hPa
(d) 08/26/1203Z, 922 hPa
(e) 08/27/0038Z, 922 hPa
(f) 08/27/0850Z, 941 hPa
(g) 08/27/1152Z, 941 hPa
(h) 08/28/0026Z, 948 hPa
(i) 08/28/1141Z, 959 hPa

Fig. 1. The microwave images of 85 - 91 GHz brightness temperature for Typhoon Nanmadol (2011). The yellow and red color areas represent the deep convective clouds of the weather system. (a) 0957 UTC 25 August; (b) 2232 UTC 25 August; (c) 0448 UTC 26 August; (d) 1203 UTC 26 August; (e) 0038 UTC 27 August; (f) 0850 UTC 27 August; (g) 1152 UTC 27 August; (h) 0026 UTC 28 August; (i) 1141 UTC 28 August. Images are available from the website of the Naval Research Laboratory, Monterey, California.

evidence for a greater amount of convection on the south and southwest sides than on the north and northeast sides. As the typhoon passed the northeastern tip of Luzon Island (Figs. 1d - f), the outer rainbands and inner-core convection strengthened over the southern side of the storm but were considerably weaker on the northern side. The storm later moved steadily northwestward toward Taiwan, and the major convection areas expanded further away from the storm center, thus increasing convection asymmetry (Figs. 1g - i). Enhanced precipitation within the southern portion of the eyewall and outer rainbands then induced heavy precipitation over southern Taiwan during its passage.

Many studies have shown that the interaction between land surface processes and topography can affect the behavior of a TC, particularly with respect to the track pattern (Brand and Blelloch 1973; Bender et al. 1987; Yeh and Elsberry 1993a, b; Lin et al. 2005; Jian and Wu 2008; Huang et al. 2011; Tang and Chan 2015), intensity change (Powell 1982, 1987; Tuleya 1994; Yang et al. 2008), rainfall distribution (Chou et al. 2011; Wang et al. 2012; Hsu et al. 2013; Yu and Cheng 2013; Chih et al. 2015), eyewall evolution and convective structure (Wu et al. 2003, 2009; Wang and Wu 2004; Chou et al. 2011; Yang et al. 2011) of the TC. The use of polar-orbiting satellite images and explicit simulations of the inner-core of landfalling storms during this decade have evidenced the evolution of the eyewall and structure of the storm. In this respect, Wu et al. (2003) used satellite observations and numerical simulations to clarify the interesting eyewall evolution of Typhoon Zeb (1998) during its passage over the Philippine's Luzon Island.

As previously mentioned, it has been proposed that terrain plays a critical role in eyewall evolution: the eyewall first contracts immediately prior to landfall, breaks down after landfall, and then reorganizes into a larger outer eyewall when the storm has returned to the ocean. Further analyses from numerical simulations have shown that both adiabatic heating and surface friction were key factors in the maintenance and reorganization of the outer eyewall when Zeb re-entered the ocean (Wu et al. 2009). Furthermore, Chou et al. (2011) used satellite microwave images to study 23 TCs that had crossed the Philippines's Luzon Island during 2000 - 2010, and they found expansion of the eyewall radius during landfall in 87% of TCs. In addition, the outer eyewall of 39% of storms re-intensified and shrank after they had re-entered the ocean; these storms redeveloped when embedding in high sea surface temperature, weak vertical wind shear, and high relative humidity environmental conditions.

There are many factors that could lead to the convective asymmetry of a TC, such as: (1) the vortex Rossby wave (Montgomery and Kallenbach 1997; Schubert et al. 1999); (2) translation speed of the TC (Shapiro 1983; Rodgers et al. 1994); (3) intrusion of dry or moist air from the environment surrounding the TC (Riemer et al. 2010; Tang and Emanuel 2010, 2012; Braun et al. 2012; Zhang et al. 2013); and (4) environmental vertical wind shear (Jones 1995; DeMaria 1996; Wang and Holland 1996; Bender 1997; Frank and Ritchie 1999, 2001; Braun et al. 2006; Xu and Wang 2013). Although all of these factors could be applied in explaining the formation of convection asymmetry in a TC, composite analyses derived from aircraft, lightning, and satellite observations show that environmental vertical wind shear is the dominant factor governing development of azimuthal wavenumber-1 convective asymmetries of TCs (Black et al. 2002; Corbosiero and Molinari 2002, 2003; Wingo and Cecil 2010; Hence and Houze 2011; Rogers et al. 2013; DeHart et al. 2014).

In the past two decades, several shear-related mechanisms have been described to explain the development of azimuthal wavenumber-1 convective asymmetries of TCs. These theories include: (1) a balanced response to a tilted vortex that produces upward motion on the downshear side (Jones 1995; Wang and Holland 1996; Frank and Ritchie 1999); (2) storm-relative asymmetric flow that produces low-level convergence and upward motion, where the relative flow is directed into the eyewall on the downshear side (Willoughby et al. 1984; Bender 1997; Frank and Ritchie 1999, 2001; Wong and Chan 2004; Braun et al. 2006; Wu et al. 2006; Xu and Wang 2013); and (3) a boundary layer thermodynamic asymmetry fuelled by surface enthalpy fluxes when air parcels travel through the right side of the shear region (Molinari et al. 2013; Zhang et al. 2013).

In this study, numerical simulations were conducted to examine the effects of topography and environmental vertical shear on Typhoon Nanmadol (2011) as it crossed the Philippine Islands. The objectives of this study were fourfold: (1) to investigate the formation mechanisms of the convective asymmetry of a storm that is embedded in environmental wind shear, (2) to understand the effects of terrain on modulation of shear-induced convective asymmetry of a land-falling typhoon, (3) to elaborate whether the adjacent weather system Typhoon Talas (2011) might affect the formation of the convective asymmetry of Nanmadol, and (4) to examine whether the simulated convective asymmetry is sensitive to the choice of model physics. The experimental design and methodology are described in section 2; results from full-physics simulations and several sensitivity experiments are discussed in sections 3 and 4, respectively; comparisons made with previous studies are highlighted in section 5; and the final section summarizes major findings and presents a proposed schematic diagram.

2. EXPERIMENTAL DESIGN AND METHODOLOGY ANALYSIS

2.1 Experimental Design

Numerical simulations are conducted with the Advanced Research Weather Research and Forecasting model, Version 3.4.1 (WRF; Skamarock et al. 2008). The non-hydrostatic WRF with three nested domains (Fig. 2) is applied to perform 72-h simulations, starting from 1200 UTC on 25 August 2011. The model was run with 40 terrain-following hydrostatic pressure coordinate vertical levels and a model top at 10 hPa. The model half-sigma levels are defined with 11 layers under 700 hPa, 17 layers between 700 - 100 hPa, and 11 layers above 100 hPa, and the lowest half-sigma level is at 0.997 and at a height of approximately 30-m. A horizontal grid spacing of the three domains is 30-km (first mesh: 330 by 160 grid points), 10-km (second mesh: 430 by 358 grid points), and 3.3-km (third mesh: 523 by 640 grid points). Two-way feedbacks are allowed between all domains. The initial and lateral boundary conditions are based on the National Centers for Environmental Prediction (NCEP) Final (FNL) Operational Global Analysis with six-hourly gridded analyses at 1.0 degree in a latitude-longitude resolution. The coupled ocean-atmosphere effect is not applied; therefore, sea surface temperature is fixed during the simulations. In addition, lower boundary conditions on sea surface temperature are initialized from the real-time, global sea surface temperature of analysis developed by the NCEP Marine Modeling and Analysis Branch. The physical schemes used in most simulations include the Grell-Devenyi cumulus parameterization scheme (Grell and Dévényi 2002), WSM5 microphysics scheme (Lim and Hong 2005), ACM2 planetary boundary layer parameterization scheme (Pleim 2007), the Dudhia (1989) shortwave scheme and the Rapid Radiative Transfer Model (RRTM) longwave (Mlawer et al. 1997) scheme. Furthermore, the cumulus parameterization scheme is turned-off in the third mesh.

To produce a storm with a realistic structure and intensity, the vortex initialization scheme is applied to all numerical experiments (e.g., Low-Nam and Davis 2001; Chou and Wu 2008; Chih et al. 2015). The bogus scheme, which includes a Rankine vortex with vortex information analyzed from JTWC Best Track data, is implanted 6 h prior to the model's initial time. A 6-h model integration is then performed to produce a spin-up, model-consistent, and asymmetric vortex structure. Finally, the model's three-dimensional control variables within a 200-km radius from the storm's center are replaced with the above spun-up vortex as the new initial condition. Note that the simulation without the storm bogusing scheme has been examined in this study, but the results are not discussed in the manuscript. However, the storm's intensity was weaker at the beginning of the period and landfall on Luzon could not be simulated, although convective asymmetry of the simulated storm was consistent with observed features.

Three numerical experiments with differing underlying surface conditions (the terrain of the Philippines, the land's surface and the ocean) are conducted to investigate the effects on modulation of shear-induced convective asymmetry of Nanmadol. The control run (CT; see Table 1 for description of all experiments) retains all the model-resolved terrain in the model domain; in the second experiment (OP), the land of the Philippines is totally replaced by the ocean, and the sea surface temperature over the Philippines is interpolated from boundary values around the replaced area; and in the third run (FP), the terrain of the Philippines is flattened to a planar area 1 m in height, but land use is the same as that used in the CT run. The aim is to examine the role of topography in the modulation of shear-induced convective asymmetries based on comparisons between CT and OP runs. The effects of surface friction and water vapor cut-off by the land's surface are compared between the OP and FP runs.

Furthermore, since the Nanmadol only passed the northeastern tip of Luzon, this situation reduces the terrain effect as compared to a typical landfalling storm. To examine this issue, two sensitivity experiments regarding implantment of a bogused vortex to southwestward of the original location of Nanmadol are conducted (CTSW, OPSW). In addition, for examining whether Talas to the east of Nanmadol might play an important role in the maintenance of uniform and robust of vertical wind shear. The CTNT sensitivity experiment, in which the circulation related to Talas is removed, is conducted to intensively study the contribution from Talas to the vertical wind shear and the related asymmetric convective structure. The metric of removal of Talas vortex is based on the procedures described on Low-Nam and Davis (2001).

A further two experiments with different model physics are also conducted to examine the sensitivity of Nanmadol's convective asymmetry formation to microphysical processes. All the physics applied in CT2 and OP2 are the same as those in CT and OP, although the Lin microphysics scheme (Lin et al. 1983) is also applied. Lin and WSM5 are both single-moment schemes; therefore, these experiments are used to compare the effect of graupel existing within the microphysics scheme. Note that the others model physics regarding planetary boundary layer processes and radiation processes are also investigated, the overall results are similar with the results of different microphysical processes. Although, many recent studies have shown that different model physics can lead to differing inner-core structures of TC simulated storms (Fovell et al. 2009, 2016; Smith and Thomsen 2010). For reducing the length of this manuscript, only the results from different microphysical processes are discussed. Detailed of the descriptions of these sensitivity experiments could be found in Table 1.

2.2 Methodology of Analysis

2.2.1 Detection of Storm Center

When the vortex of a simulated storm is influenced by topography, its center cannot easily be identified based on the location of minimum sea level pressure or the center of circulation near the surface, and is instead defined by the circulation center of the 850-hPa streamlines. In addition, the vortex tilting distance is calculated based on the displacement between 200- and 850-hPa circulation centers.

2.2.2 Calculation of Vertical Wind Shear

In global analyses and model simulations, the values of environmental vertical wind shear near the core of a TC are calculated using the vector difference between the non-axisymmetric winds at 200- and 850-hPa and averaged within an annulus extending 2 - 8° from the storm's center. To ensure that shear values are not corrupted by the vortex itself, the method of shear calculation used here is the same as that used in Knaff et al. (2005). The non-axisymmetric wind is calculated for total wind, where the symmetric component of the vortex for the area around the 0 - 8° radius of the storm is removed. Note that the different metrics of vertical shear calculation are also examined, such as the calculation area and whether or not vortex removal is applied. The results of all experiments in this study show only slight changes in the overall (time-averaged) vertical shear vectors (magnitude < 1 m s^{-1}, angle < 10°) (figures not shown).

2.2.3 Calculation of Storm-Relative Flow

In this paper, most analyses are conducted using storm-relative coordinates. Following the method in Bender (1997), the storm-relative flow ($\mathbf{V}_{rel}$) is defined as $\mathbf{V}_{rel} = \mathbf{V} - \mathbf{C}$, where $\mathbf{V}$ is the model horizontal wind field, and $\mathbf{C}$ is the storm's translation speed (determined by computing the moving speed of the TC using the location displacement of the storm's center over the previous three hours).

2.2.4 Definition of Shear-Relative Quadrants

This paper discusses six classifications of the quadrant-averaged metric: downshear-left (DL), downshear-right (DR), upshear-left (UL), upshear-right (UR), downshear (DS), and upshear (US) quadrants. The quadrant-averaged ($\overline{A}$) metric is calculated as,

$$\overline{A} = \frac{\int_{\theta_0 - \frac{\pi}{4}}^{\theta_0 + \frac{\pi}{4}} A d\theta}{\int_{\theta_0 - \frac{\pi}{4}}^{\theta_0 + \frac{\pi}{4}} d\theta} \tag{1}$$

where A is any scalar variable, and θ_0 is the middle angle of the desired quadrant. For example, θ_0 is the angle of the shear direction (θ_s) for the DS quadrant, and $\theta_0 = \theta_s + \dfrac{\pi}{4}$ for the DL quadrant.

3. RESULTS

3.1 Track and Intensity

Figure 3 shows comparisons between the track and intensity determined in three simulations Typhoon Nanmadol and those of JTWC's best track. In the CT run, although the translation speed of the simulated storm is slightly slower than the observed one, the simulated track is very close to that of JTWC; the model not only captures the overall northwestward movement of Nanmadol but also simulates landfall over the northeast coastline of the Philippines. However, for the OP and FP runs, the simulated tracks show a rightward (cross-track) bias during the simulation period, where the rightward bias in the FP run is more obvious than that in the OP run. The slight discrepancy of simulated tracks between the three experiments could be related to the influence of Luzon topography on the steering flows of the storm; this effect is also revealed in the simulation results of Wu et al. (2009). Furthermore, the storm translation speed in the OP run is much faster than that in FP run, which could cause the storm to be influenced more by the topography of Taiwan during the later simulation period. This study focuses on convection asymmetry and therefore does not include a detailed examination of steering flow differences in these experiments.

Vortex implementation used in the CT run enables the model storm to reach the correct intensity, and a steady-state minimum sea-level pressure near to 920-hPa was maintained at the beginning of the 24-h simulation, which is very close to the official value reported by the JTWC. Thereafter, the model storm was gradually influenced by the topography of both the Philippines and Taiwan, and thus the storm intensity decreased steadily throughout the entire simulation period. Overall, with the exception of the initial time, the intensity difference between the CT run and the official report is approximately 10-hPa throughout the simulation period, and the 0 - 72 h mean absolute intensity difference between the CT run and the official report is 10.0 hPa.

For the OP run and the FP run, the simulated storm gradually intensified from the beginning until 42 h and then weakened. The storm translation speed is much faster in the OP run, thus leading to a more obvious weakening of the storm during the later simulation period. Overall, the evolution intensity of the OP run and FP run are stronger than that of the CT run. This result is reasonable; the model storm gains more energy from the ocean's surface, which led to the higher intensity in the OP run.

The model simulates the track and intensity evolution of Typhoon Nanmadol reasonably well during the 72-h simulation period in the CT run, and thus able to provide high spatial and high temporal resolution simulation data for use in examining mechanisms relating to the influence of the environmental vertical wind shear and topography on the formation of the Nanmadol's convective asymmetry.

3.2 Convective Structure and Vertical Shear Analysis

The model adequately simulates the steady-state

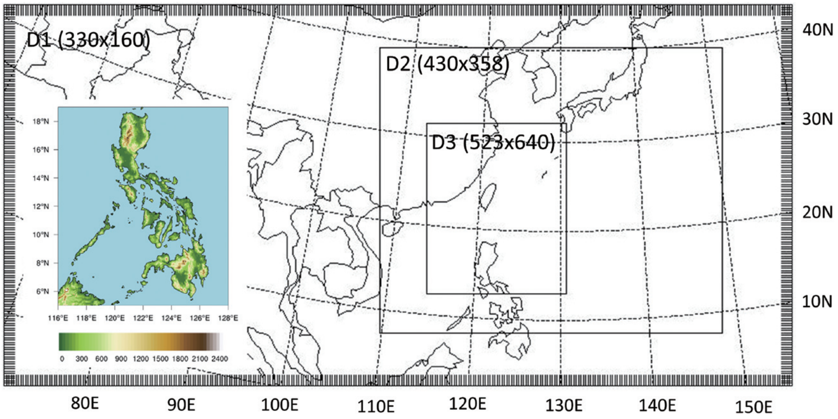

Fig. 2. The triply nested WRF domains at horizontal grid size of 30, 10, and 3.3 km, respectively. The terrain height of 30-min USGS (United States Geological Survey) of the Philippines was also plotted and overlaid on the lower-left corner for reference (unit: m).

Table 1. Summary of the numerical experiments in this study.

Experiment	Description	Philippine terrain	Philippine land use
CT	Control run	Yes	Yes
OP	Ocean run	virtual ocean	virtual ocean
FP	Flattened terrain run	1-m height	same as CT
CTSW	Same as CT, except the bogused vortex was implanted to the southwest of original reported location (2° southward and 1° westward)	Yes	Yes
OPSW	Same as OP, except the bogused vortex was implanted to the southwest of original reported location (2° southward and 1° westward)	virtual ocean	virtual ocean
CTNT	Same as CT, except the vortex of Typhoon Talas (2011) was removed	Yes	Yes
CT2	Same as CT, except the Lin microphysics scheme is adapted	Yes	Yes
OP2	Same as OP, except the Lin microphysics scheme is adapted	virtual ocean	virtual ocean

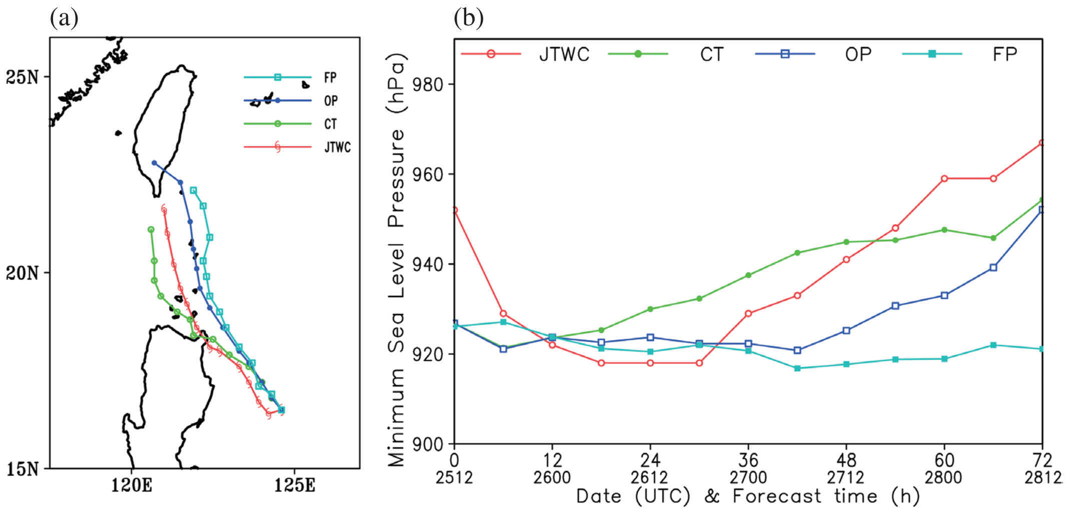

Fig. 3. (a) Best track of JTWC and model tracks of CT, OP, and FP experiments, note that the track point before 12 h in CT run is overlapped with OP and FP runs; (b) minimum sea level pressure of Typhoon Nanmadol (2011). The data are plotted for every 6 h.

azimuthal wavenumber-1 convective asymmetry during the entire simulation period, as shown in the simulated reflectivity of Fig. 4. Before making landfall, (Figs. 4a - c), the inner-core elliptical eyewall and outer spiral rainband over the west part of storm were clearly simulated. Note that the outer spiral rainband over the western part of the storm is also evident in satellite images (i.e., Fig. 1b), and the very active convection over the southern part of the storm has already shown during this period. Convection asymmetry becomes more obvious during the storm's passage over the island (Figs. 4e - f), the outer rainbands over the northeastern part of the storm were gradually suppressed and those located over the southwestern part were considerably enhanced. Asymmetric convection becomes more evident after the storm exits Luzon Island (Figs. 4g - i), the northern eyewall erodes significantly and the high reflectivity area over the northeastern part of the storm declines. This paper subsequently illustrates that evolution of this asymmetric convection is highly related to the environmental vertical wind shear, while the influence of terrain is negligible. How terrain contributes to the asymmetric convention of Nanmadol is examined in the following section.

Based on the evolution of these reflectivity images, the inner eyewall of the storm gradually weakens but does not break down, while the outer rainband forms and gradually organizes during the storm's passage over Luzon Island. However, the outer rainband is never organized to the outer eyewall, and therefore, the concentric eyewall of the storm scenario is not revealed in the control simulation. This detailed structural evolution of the inner-core structure is

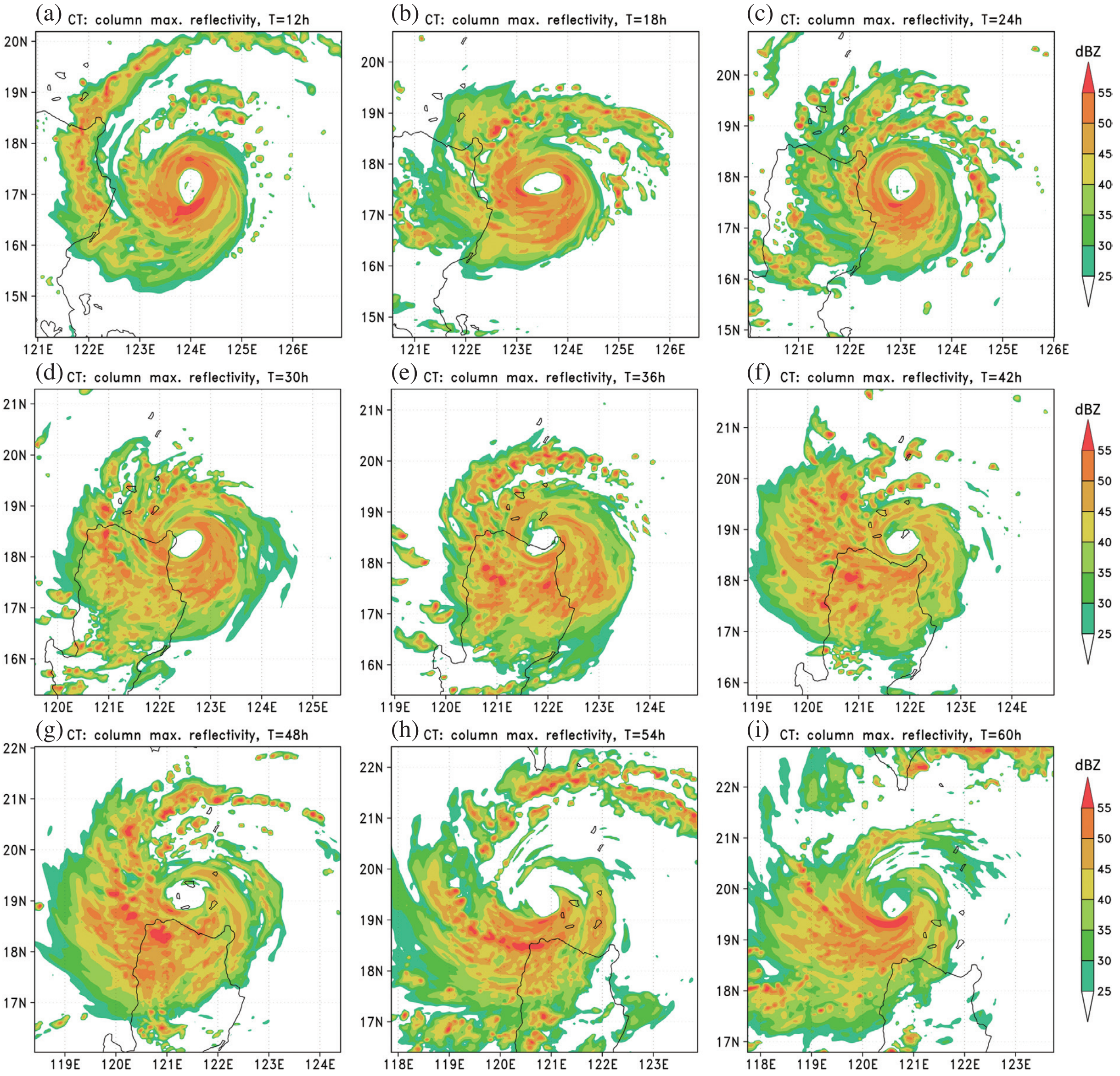

Fig. 4. The column maximum reflectivity (unit: dBZ) in CT run. The data are plotted from the 3.3-km grid domain.

consistent with observations, as shown in Fig. 1. Recent studies (Wu et al. 2003, 2009; Chou et al. 2011) have shown that a terrain-induced eyewall evolution can be found in storms embedded under favorable environmental conditions (e.g., high sea surface temperature, low vertical wind shear, and high humidity). The inner eyewall does not break down, and this is probably due to the influence of high vertical wind shear and the minor interaction of TC inner-core with topography when Nanmadol passed the northeastern tip of Luzon Island; therefore, eyewall evolution of Nanmadol is not observed during its passage over the Philippines.

Figure 5 shows a comparison between vertical wind shear in NCEP global analysis and the model simulation, and simulated 200- and 850-hPa winds at simulation times of 12 and 60 h. The storm was embedded in a northeasterly environmental shear, which is evident in both the analysis and simulations (Figs. 5a - d). This northeasterly shear was mainly originated from the lower level monsoon gyre flows over the Northwestern Pacific, which covered almost the entire analyzed domain, and an upper synoptic anticyclonic system was located over the northeast of Nanmadol (Figs. 5e - h). The storm located to the east of Nanmadol was Typhoon Talas (2011), which also showed an obvious asymmetric convection around the eyewall and spiral rainband areas. These strong convective areas were also located over the southern part of the storm, and the environmental vertical wind shear was also within a northeasterly wind shear caused by the fact that the storm was embedded in a monsoon gyre system. This asymmetric convection of Talas again demonstrates that the northeasterly environmental shear induced some southern-enhanced convection for TCs over the Northwestern Pacific Ocean.

Figure 6 shows comparisons between the shear vector in the CT simulation and NCEP analysis. The simulated shear direction is in a quasi-steady-state easterly direction, which is close to that of NCEP analysis, although a slight clockwise bias is found in the simulation. However, the simulated shear magnitudes are much larger than those in the analysis. The shear magnitudes of the simulation in the initial period (0-24-h) are approximately 5 - 10 m s^{-1}, which is consistent with analysis, while the values at a later time (48-60-h) are 15 - 20 m s^{-1}, which represents approximately double the values obtained from NCEP analysis (Fig. 6a). This discrepancy between the simulation and analysis is a result of a narrow upper-level anti-cyclonic system located north-east of Nanmadol, which could not be accurately simulated by the model. The model tends to simulate a much larger and stronger anti-cyclonic system over the upper troposphere during the later simulation period, and thus increasing the westward component of the vertical wind shear (i.e., Figs. 5f, 6b - d). Note that even when the model is initialized by 0.75° × 0.75° ERA-Interim global analyses, the model overpredicted the upper-level anti-cyclonic system and failed to solve the eastward bias of the shear patterns.

3.3 Analysis in a Storm-Relative Coordinate

Figure 7 shows the 12-60-h time-averaged composite of simulated upper-level and low-level storm-relative flows, midlevel vertical velocity and column-maximum reflectivity around the inner core of the storm. Note that the results at any individual time are similar to the composited results (figures not shown). The upper-level flow appears as cyclonic circulation around the storm, and both the radial velocity and tangential velocity have an asymmetric distribution (Figs. 7a, b). The area with a higher radial outflow appears on the downshear side, while the area with smaller radial inflow forms on the upshear side. However, the areas with larger and smaller tangential velocities are different from those of the radial velocities: the area of high (low) tangential velocity occurs in the upshear-right (upshear-left) quadrant of the storm. With respect to low-level storm-relative flows (Figs. 7c, d), a much higher cyclonic flow is found at a low level, and asymmetric patterns of radial and tangential velocities are also revealed. A stronger radial inflow appears on the downshear side, while a weaker radial inflow is formed on the upshear side. The asymmetric pattern of the low-level tangential velocity is not as clear as the radial velocity, but the stronger tangential velocity area appears on the upshear side and the weaker tangential velocity on the downshear side. For middle-level vertical velocity and reflectivity (Figs. 7e, f), areas with higher vertical motion and reflectivity are located in the southwestern and southern part of the storm (the downshear to downshear-left area). Furthermore, the area of higher reflectivity is formed further downwind of the storm circulation than that of high vertical velocity. The relationships between the 200-hPa, 850-hPa non-axisymmetric wind and vertical shear vector could also be examined in Fig. 7e. It is found that most of the shear vectors around the storm are easterly which are similar with the direction of synoptic vertical wind shear calculated from 2 - 8° annular average. In addition, the results showed that these easterly shear vectors are resulted from the low-level eastward non-axisymmetric wind and upper-level westward non-axisymmetric wind.

Figure 8 shows the along-shear, vertical cross-section plot of radial flow and the vertical circulation wind vector at 12, 24, 36, 48, and 60 h, as well as the time-averaged composites between 12 - 60 h. There is little variation in the shear direction during the simulation period (meteorological angle ranges from 230 - 280°, where angle is calculated clockwise with zero at the north and 0° represents southward wind vector). Therefore, an angle of 260° obtained from the 0-60-h time-averaged vertical wind shear direction is chosen for the vertical cross-section. From the start of the simulation, a thick, strong low-level inflow (upper-level outflow) layer is clearly visible over the downshear side, while a thin and weak low-level inflow (upper-level outflow) layer can be seen over the upshear side (Fig. 8a).

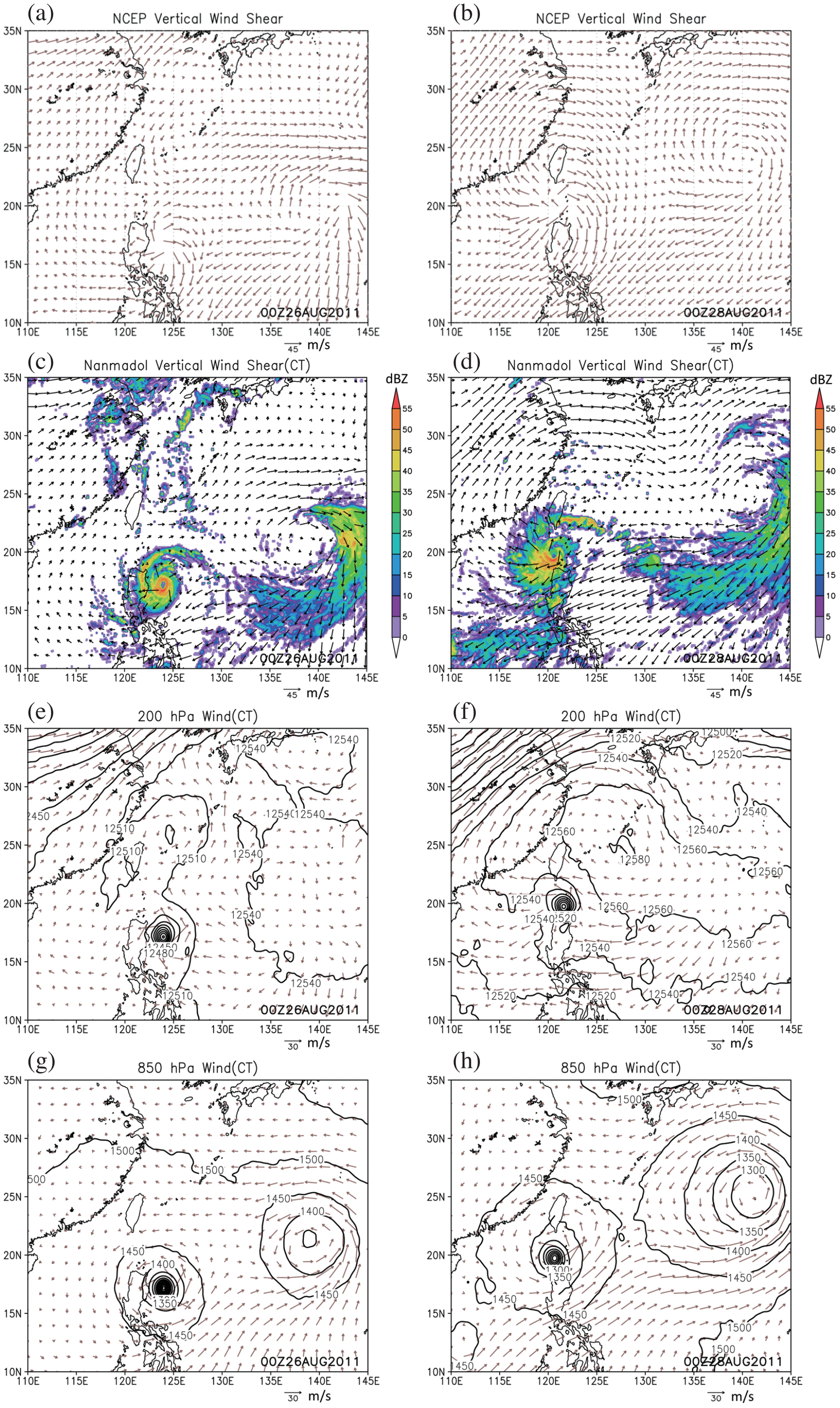

Fig. 5. Horizontal distributions of NCEP analyses and simulations of CT run at 0000 UTC 26 August 2011 (left panels) and 0000 UTC 28 August 2011 (right panels). (a) and (b) vertical wind shear of NCEP analyses; (c) and (d) simulated vertical wind shear and column maximum radar reflectivity (shaded, unit: dBZ); (e) and (f) simulated wind vector and geopotential height (contour, unit: gpm) at 200 hPa; (g) and (h) same as (e) and (f) but for 850 hPa. The model simulation data are from the 10-km grid domain. Unit of wind speed is m s^{-1}.

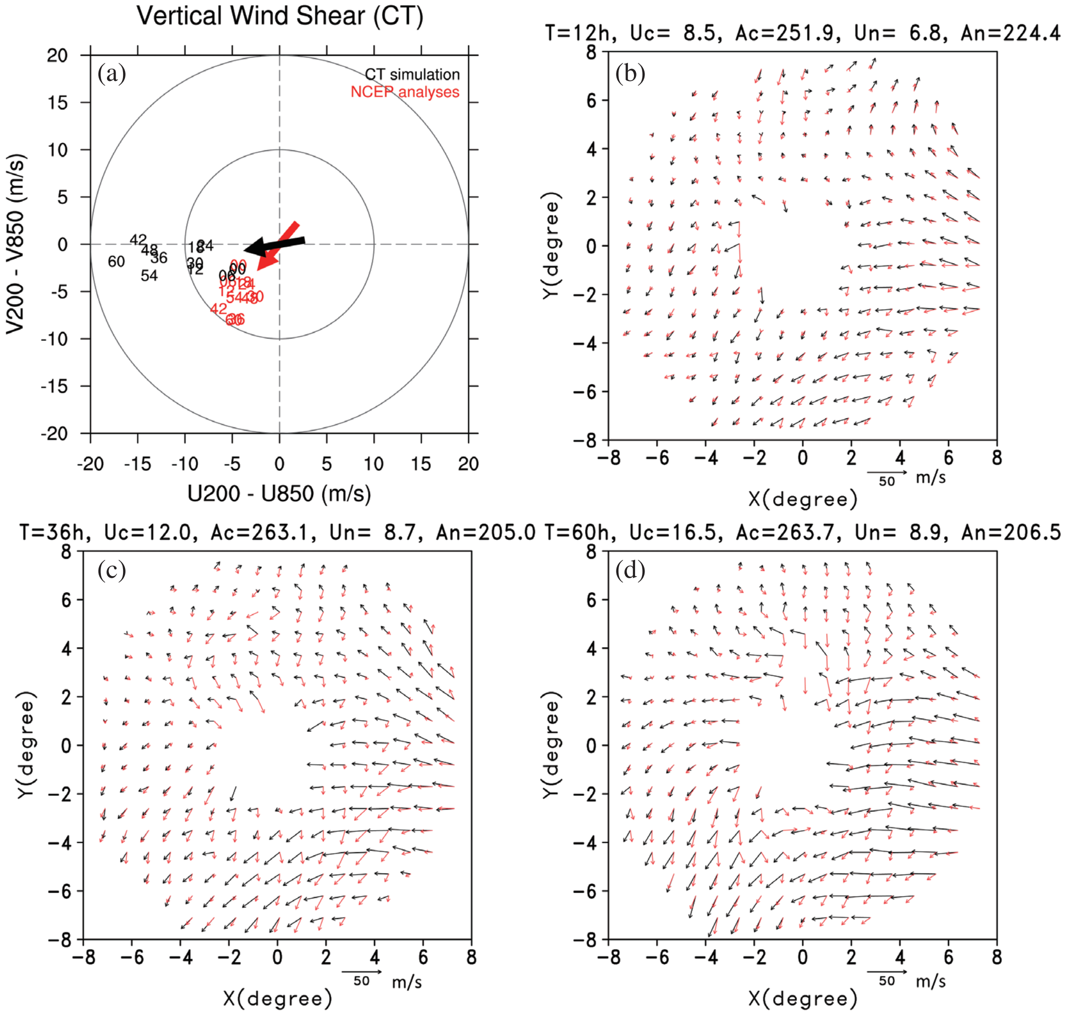

Vertical Wind Shear (CT)

T=12h, Uc= 8.5, Ac=251.9, Un= 6.8, An=224.4

T=36h, Uc=12.0, Ac=263.1, Un= 8.7, An=205.0

T=60h, Uc=16.5, Ac=263.7, Un= 8.9, An=206.5

Fig. 6. The vertical wind shear of CT simulation and NCEP analysis, unit in m s^{-1}. (a) The two-digital value represents the analysis or forecast time which begins from 1200 UTC 25 August 2011. Black arrow denotes the 0-60-h time-averaged vertical wind shear direction (260°) of the simulation, and red arrow represents the 0-60-h time-averaged vertical wind shear direction (220°) of the analysis. (b) - (d) show the vertical wind shear vector of simulation (black vector) and analysis (red vector) for areas within 2 - 8 radii at 12, 36, and 60 h respectively. Uc (Un) and Ac (An) denote the magnitude and direction of the area-mean of the shear vector for simulation (analysis). The 10-km-resolution simulation and 1-degree-resolution analysis are interpolated to a 5-km by 5-km storm-relative coordinate for the vertical shear calculation.

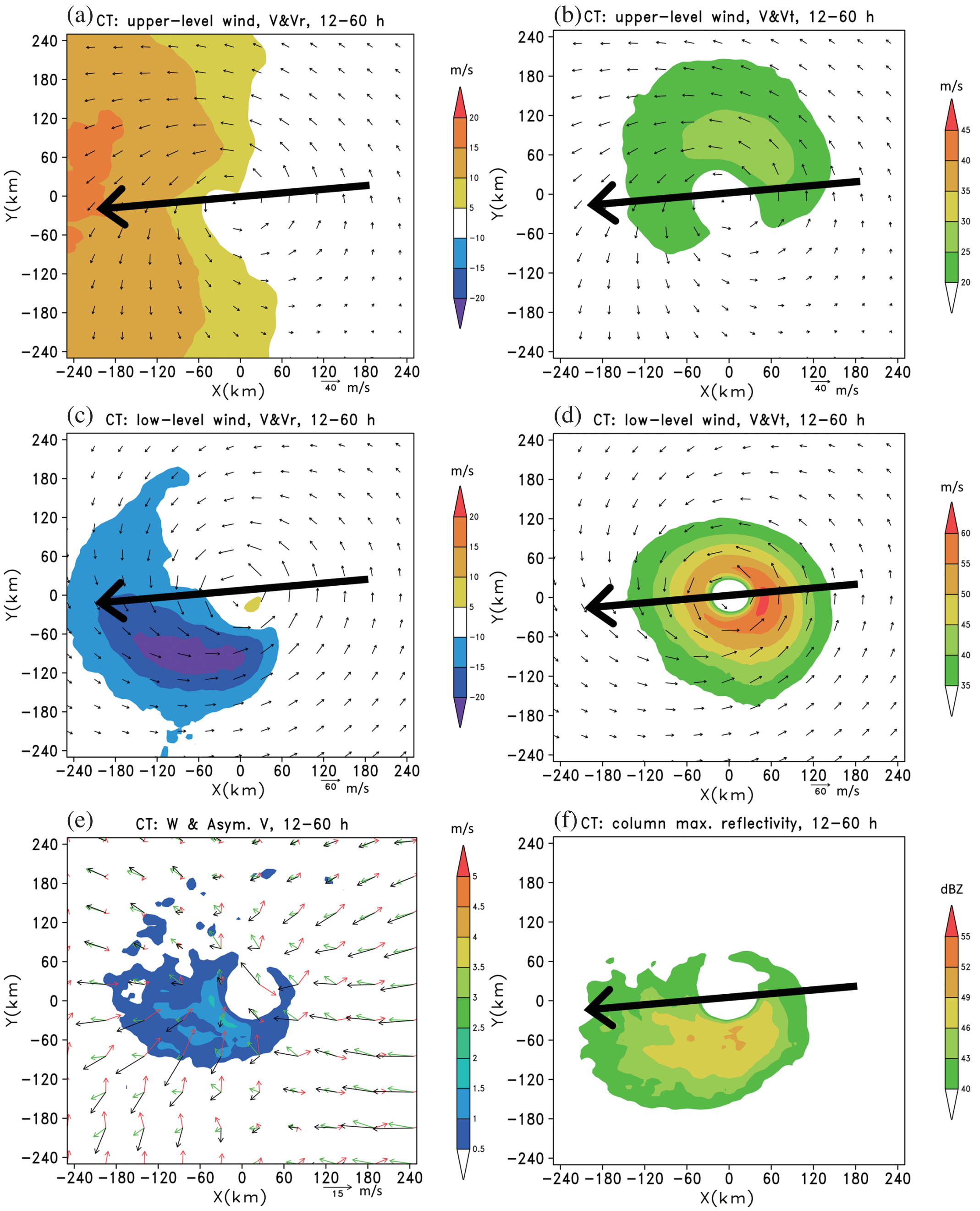

Fig. 7. The 12-60-h time-averaged horizontal distribution of simulated storm-relative flows, vertical velocity, and column-maximum reflectivity for CT experiment. (a) Upper-level wind vector and radial velocity, (b) upper-level wind vector and tangential velocity; (c) and (d) same as (a) and (b), but for low level; (e) midlevel vertical velocity (shaded), 200-hPa (green vector) and 850-hPa (red vector) non-axisymmetric wind, and vertical wind shear vector (black vector); (f) vertical-column maximum reflectivity (unit: dBZ). The low-level, midlevel, and upper-level is defined as the vertical averaged at 1000 - 800, 800 - 300, and 300 - 100 hPa, respectively. Unit of wind speed is m s^{-1}. Black vector denotes the vertical wind shear direction (260°) calculated from the 10-km grid domain of the CT run.

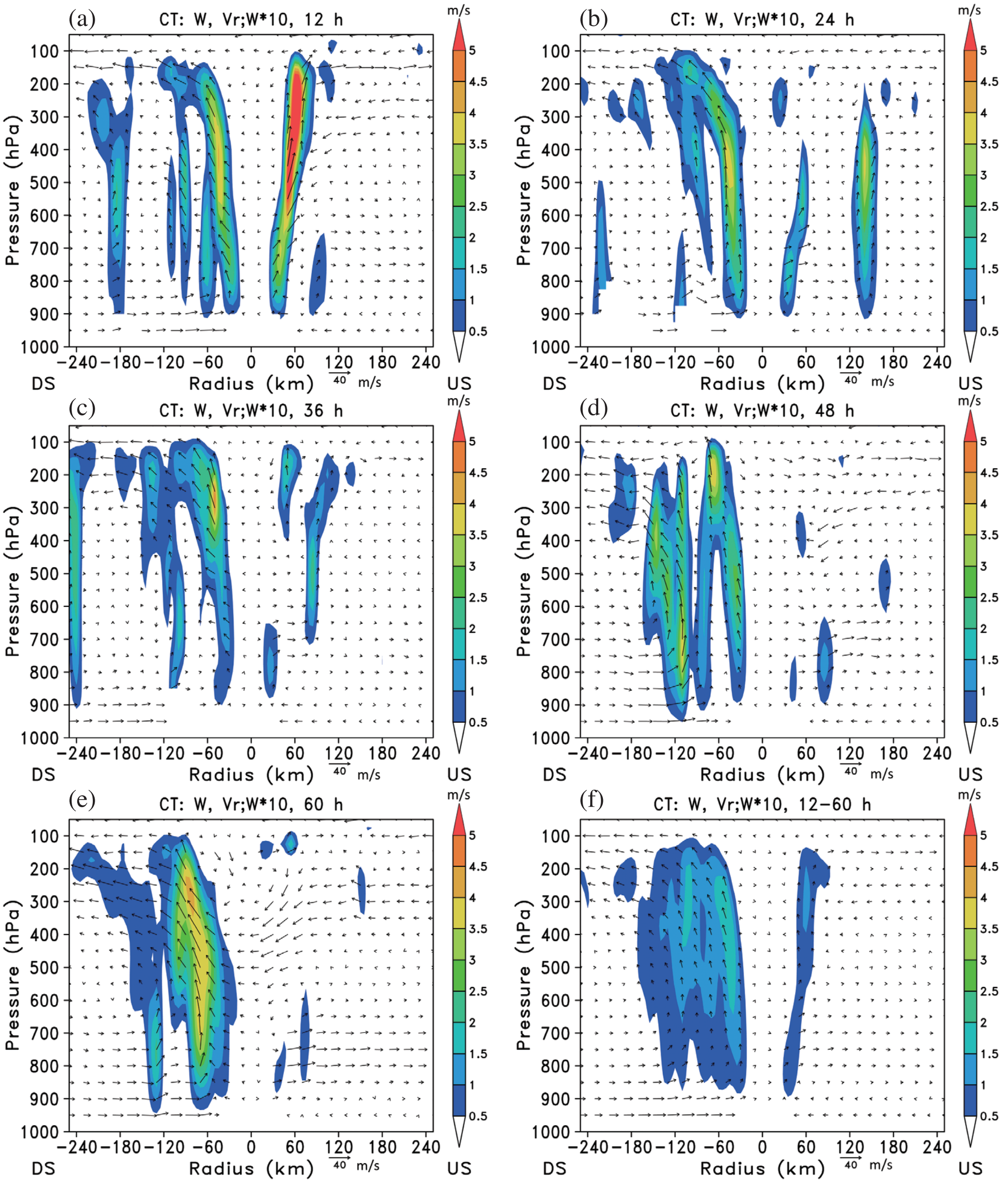

Fig. 8. Vertical cross-section along the shear direction of vertical velocity and the secondary circulation wind vector for CT run. (a) at 12 h, (b) at 24 h, (c) at 36 h, (d) at 48 h, (e) at 60 h, (f) 12-60-h time-averaged. The secondary circulation vector is composed with radial velocity and vertical velocity, and the magnitude of vertical velocity is multiplied by ten. The angle of the cross section in (a) - (f) is based on the 0-60-h time-averaged vertical wind shear direction as shown in Fig. 7f.

Furthermore, in the deep and strong low-level inflow and upper-level outflow regions, high vertical motion extending from the inner to the outer core of the storm is also revealed. However, vertical motion is relatively weak in the region of thin and weak low-level inflow and upper-level outflow. The same features are also shown at 24-, 36-, 48-, and 60-h simulation (Figs. 8b - e) and in the 12-60-h composited result (Fig. 8f). The existence of a slight outflow layer (900 - 700 hPa) and inflow layer (400 - 200 hPa) in the radii of 60 - 240 km away from the storm center are noted, which become more obvious later over the upshear side (Fig. 8e); these flows thus decrease the low-level inflow and upper-level outflow strength over the upshear side. Based on the vertical cross-section analyses, the inner-core vertical motion of the storm is seen to be strongly connected to the thickness and strength of the storm's low-level inflow and upper-level outflow.

3.4 Analysis of Storm's Primary and Secondary Circulation

To quantitatively examine the differences between the storm's relative flows in the shear-relative quadrants, the 12-60-h time-azimuthally averaged primary circulations (tangential velocity) and secondary circulations (radial and vertical velocities) of the storm at the DL, DR, UL, UR, DS, and US quadrants are calculated. In comparison of primary circulation between the six different quadrants (figures not shown), the tangential wind of the entire vortex scale is roughly as same as the maximum tangential velocity at the top of the boundary layer. In addition, a higher maximum tangential velocity (> 60 m s^{-1}) is found at the top of the boundary layer in the UL quadrant, which is consistent with the composited result of low-level tangential wind, as shown in Fig. 7d.

However, the secondary circulation patterns are very different among the quadrants, and can be classified as belonging to either (Fig. 9) the downshear side, as stronger secondary circulations are found in DL, DR, DS quadrants (Figs. 9a, b, and e) or to the upshear side, as relatively weaker secondary circulations are revealed in UL, UR, US quadrants (Figs. 9c, d, and f). It is clearly shown that the thickness and strength of the low-level inflow and upper-level outflow, as well as the width and strength of the mid-level upward motion are stronger over the downshear side than over the upshear side. Moreover, the strongest and weakest low-level inflows are located in the DL and UL quadrant, while the strongest and weakest upper-level outflows appear in the DR and UL quadrants, respectively. Simulations also show a local, higher, vertical velocity area located over the upper-level eyewall in the DR quadrant, where the upper-level outflow is also stronger than in other quadrants. Note that two local maximum vertical velocity areas are located at both the eyewall and outer-core of the storm in the DL and DR quadrants, which are the result of the active outer rainband formed over the downshear side. This slight variation of the inner-core structure is also revealed in both horizontal reflectivity and vertical cross-section images, as shown in Figs. 4 and 8, respectively.

4. SENSITIVITY EXPERIMENTS

4.1 Terrain Sensitivity Experiments

To examine whether Philippine Island topography played any role in affecting the convective asymmetry of Nanmadol, two terrain sensitivity experiments were conducted. It was expected that the role of topography in modulating shear-induced convective asymmetries could be examined based on comparisons between the CT and OP runs, and the effects of surface friction and water vapor cut-off by land surface could be discussed using comparisons between the OP and FP runs. However, the vertical wind shear patterns and composited results of the horizontal distribution of upper-level and low-level relative-flows, vertical motion and simulated reflectivity were generally the same in OP, FP, and in the CT run (figures not shown). Therefore, the evolution of simulated reflectivity and the composites of the secondary circulations within different shear-relative quadrants are focused on here.

Figure 10 shows horizontal distributions of simulated reflectivity from the OP and FP runs during 24 - 60 h. Results of the CT run are also compared (Figs. 4c, e, g, and i), and overall convection asymmetries are revealed in both the OP and FP runs. However, the degree of asymmetry is much smaller at the beginning of the simulation, and it enlarges later. In addition, certain differences are noted between the inner-core of the storm in the CT, OP, and FP runs: the eye size is the smallest in the CT run and largest in the OP run at 36- and 48-h of simulation time. This difference is due to the eyewall contraction effect of the landfalling storm (Wu et al. 2003, 2009; Chou et al. 2011). In the CT run, the simulated storm makes landfall, thus the friction effect is more obvious than in the other simulations, and contraction of the eyewall is more evident. Topography was removed in the OP run simulation, and the eyewall contraction induced by topography is not evident, which thus led to a larger eye size. Furthermore, the friction effect in the FP run from the 1-m land surface also leads to a slightly smaller eye size compared to that of the OP run. Since more friction effect from the land surface induces larger radial inflows over the boundary layer, thus leads the contraction of the eyewall. This tiny difference of the eyewall evolution between the 1-m land surface and ocean surface is also consistent with results reported in previous studies (Wu et al. 2009; Chih et al. 2015).

For an improved objective comparison of the differences between the CT, OP, and FP runs, composites of midlevel vertical velocity and a vertical cross-section along the shear direction are illustrated during the period of the storm's

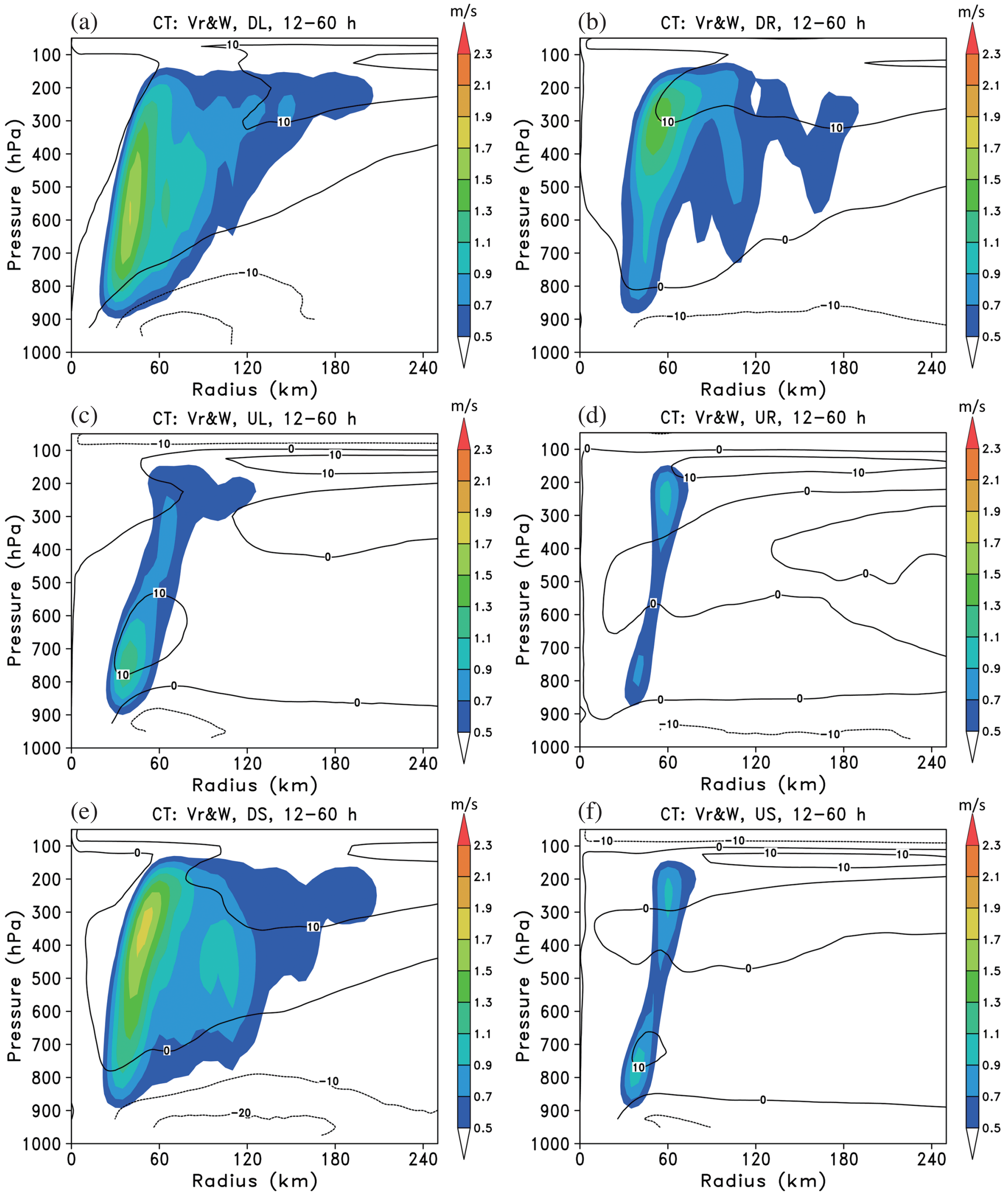

Fig. 9. Time- (12 - 60 h) and quadrant-averaged radius-height plot of radial velocity (contour) and vertical velocity (shaded) for CT run. (a) Downshear-left quadrant, (b) downshear-right quadrant, (c) upshear-left quadrant, (d) upshear-right quadrant, (e) downshear quadrant, (f) upshear quadrant. Unit is m s^{-1}.

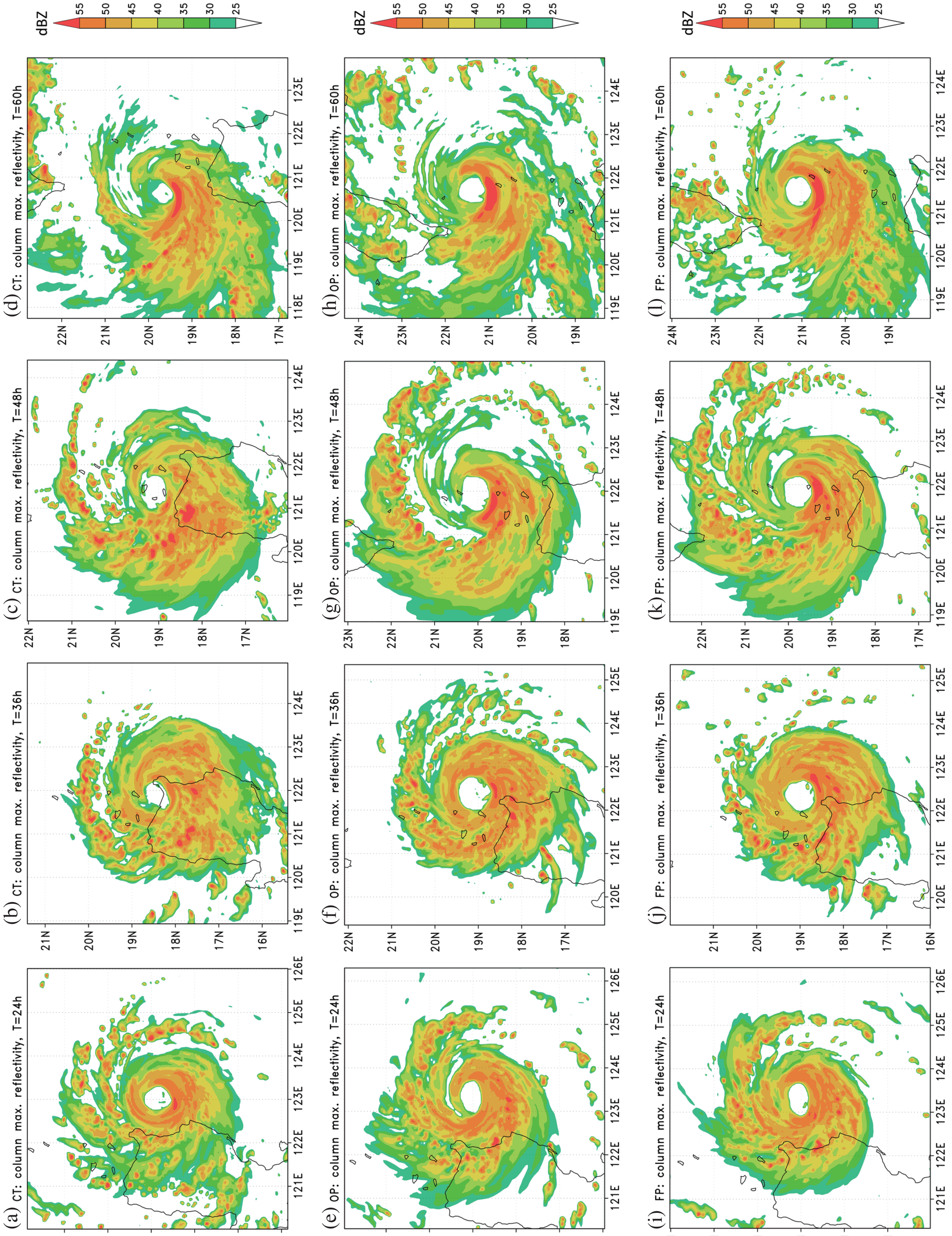

Fig. 10. Same as Fig. 3 but plotted from 24 - 60 h by every 12 h for CT run (upper panels), OP run (middle panels), and FP run (lower panels).

closest proximity to Luzon Island (Fig. 11). Note that the 0-60-h composited vertical wind shear are almost same for the three runs (magnitude difference < 1 m s^{-1} and angle difference < 5°), and the angle of the vertical cross-section in Figs. 11b, d, f is also chosen as 260° for both the OP and FP runs. Overall, the asymmetric vertical velocity patterns are very similar to the results of simulated reflectivity (Fig. 10). Although there are slight differences among the three experiments, the high vertical velocity areas are located on the downshear side. In the CT run (Fig. 11a), it is suggested that topography exerts a blocking and friction effect, which resulted in a much weaker storm intensity that leads to considerably reduced vertical velocity of the simulated storm. Furthermore, a much smaller eye size is also found in the composite. The OP run (Fig. 11c) has no blocking and friction effect from topography, and a stronger storm intensity is obtained, which leads to more intense eyewall and rainbands with higher rainfall rate over the downshear side.

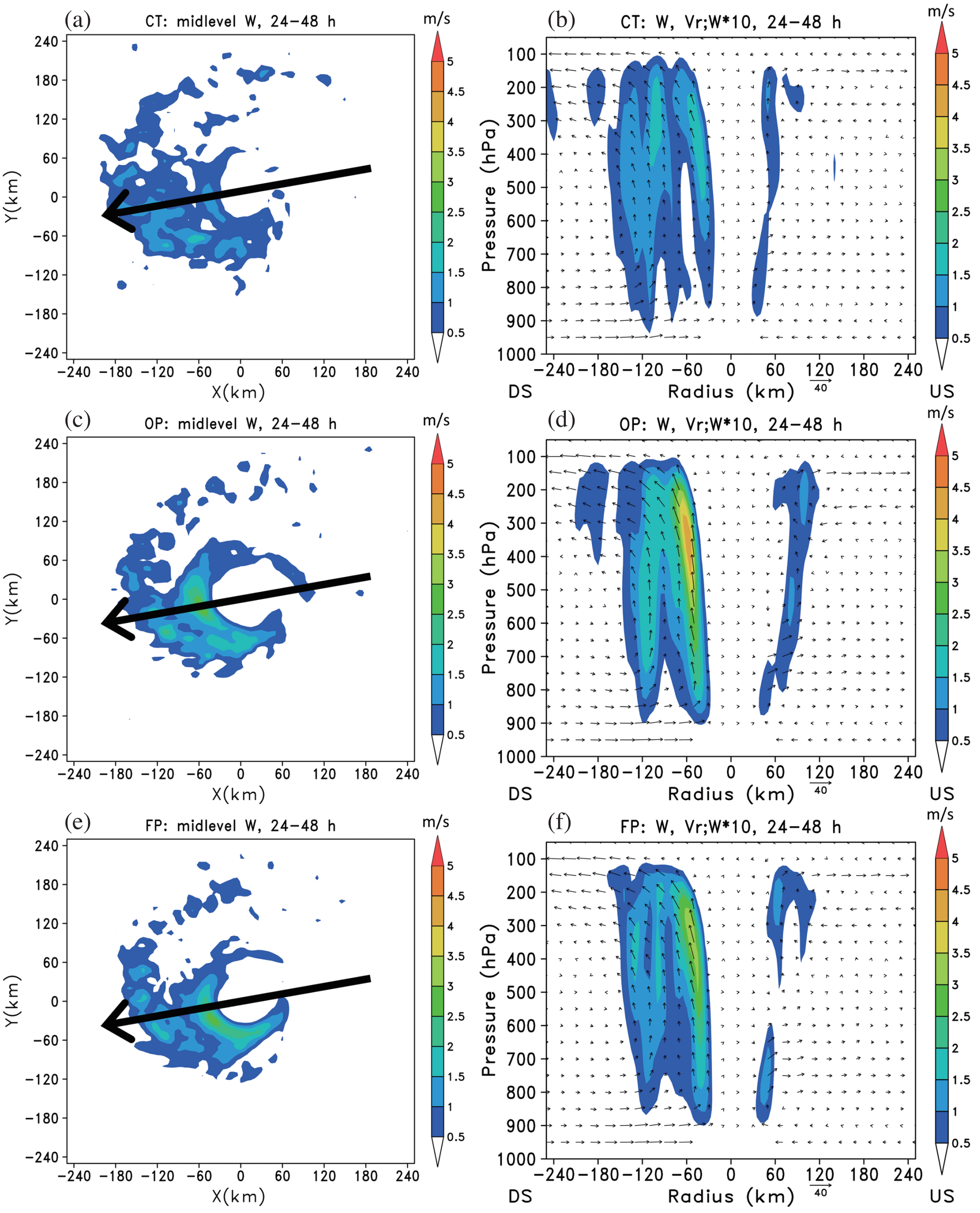

Fig. 11. The time-averaged (24 - 48 h) horizontal distribution of simulated midlevel vertical velocity (left panels, same as Fig. 8e), and vertical cross-section along the shear direction of vertical velocity and the secondary circulation wind vector (right panels, same as Fig. 9f) for CT, OP, and FP run. Black vector denotes the 24-48-h time-averaged vertical wind shear direction (260°) calculated from the 10-km grid domain of the CT run.

The minimal friction effect in the FP run (Fig. 11e) also results in a much greater storm intensity and intense inner-core vertical velocity over the downshear side. For the time-averaged vertical cross-section analyses of three experiments (Figs. 11b, d, and f), asymmetric secondary circulations are generally evident in all three experiments. In all three runs, a stronger and thicker low-level inflow, upper-level outflow layers, and a broader updraft are observed on the DS side, whereas the thickness of the inflow and outflow layers and breadth of the updraft exhibits an obvious decrease on the US side. Furthermore, the low- to midlevel inflow (~700 hPa) and mid- to upper level inflow (~300 hPa) over the US also appear. The only difference between the three experiments is the strength of the secondary circulation, which is highly correlated with the simulated storm's intensity.

The slight difference in the inner-core structure between the three experiments can be assessed by plotting the composite differences in vertical velocity and secondary circulation, as shown in Fig. 12. The blocking and friction effect of the topography is clearly revealed from comparisons between the CT and OP run (Figs. 12a, b). Areas with a positive-value (more upward motion) are located around a 30-km radius near the storm's center and at 120 - 180 km on the downshear side of the storm center, whereas obvious negative-value (less upward motion) are apparent around a 60-km radius near the storm's center. These areas also extend from the low troposphere to the upper troposphere. Such features indicate that the existence of the topography could lead to contraction of the inner eyewall and further expansion of the outer rainband or convection over the terrain-influenced area. Meanwhile, the friction effect of the land surface of Luzon Island is evidenced in a comparison between the FP and OP runs (Figs. 12c, d). The major difference is located at a 30 - 120 km radii from the storm's center: two obvious rings with positive and negative vertical velocity differences are located roughly at a 60- and 90-km radius, respectively; these areas also extend from the low to upper troposphere. Again, these features show that the simulated eyewall of FP run was further contracted due to the 1-m planar land surface of Luzon Island. Furthermore, no significant differences can be seen between the FP and OP runs for the outer part of storm (> 120-km radius).

For examining the typical topography effect of a landfalling storm on high-elevation terrain, the bogused-vortex was implanted to southwestward of original reported location, thus leads to the storm could pass the main topography

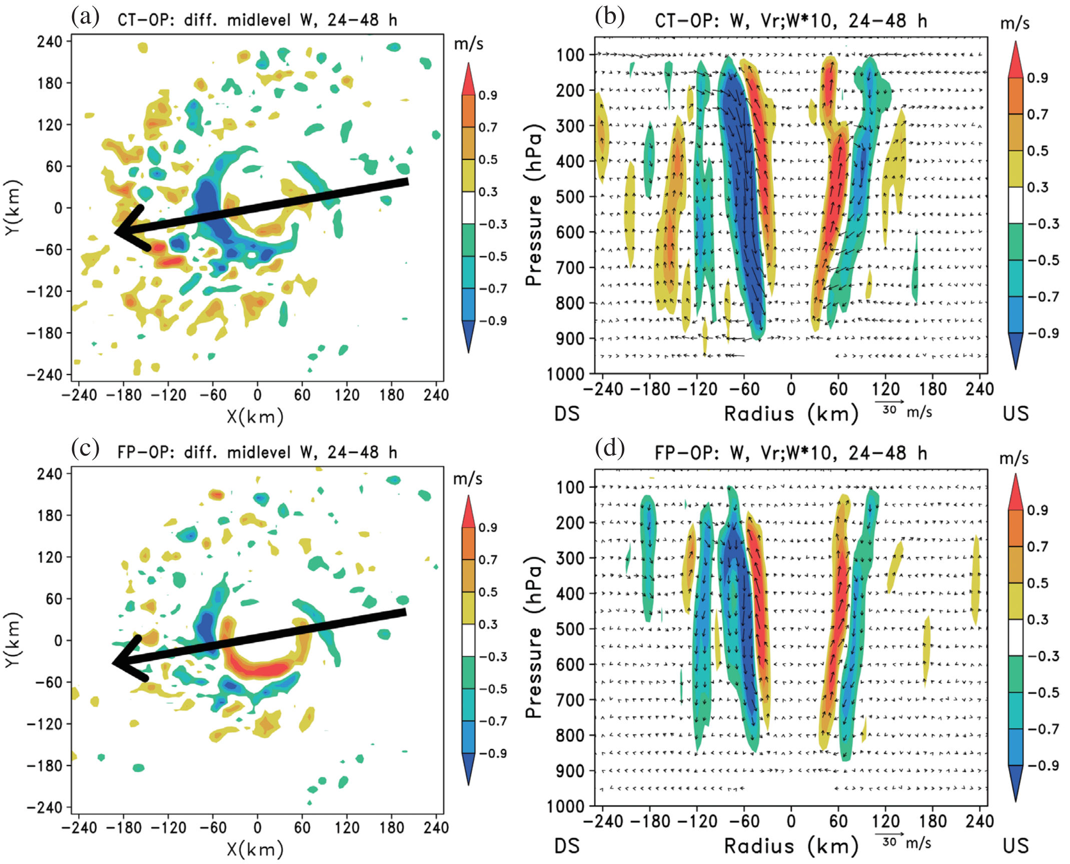

Fig. 12. The difference of time-averaged (24 - 48 h) midlevel vertical velocity (left panels) and vertical cross-section along the shear direction of vertical velocity and the secondary circulation wind vector (right panels). (a), (b) CT minus OP run; (c), (d) FP minus OP run. Unit is m s^{-1}. Black vector denotes the 24-48-h time-averaged vertical wind shear direction (260°) calculated from the 10-km grid domain of the CT run.

of Luzon. Figure 13 shows the simulation results of CTSW and OPSW sensitivity experiments. Although the metric to implant a vortex to different location leads obvious imbalance in the model, after the first 12-h model spin-up, both the track and intensity evolution are reasonable during the later period (Figs. 13a, b). For CTSW run, the simulated track passes the high terrain area of northern Luzon, the inner-core of storm was affected by the topography for more than 12 h. The intensity decreases at least 30 hPa after crossing the Luzon. For OPSW run, the track is also closer to the Luzon and the intensity evolution is slightly stronger than OP run. The vertical wind shears of CTSW and OPSW runs during terrain-influenced time are also similar to the CT and OP runs. The 24-48-h composited shear magnitude (direction) is 8.7, 8.7, 9.2, and 8.3 m s^{-1} (260, 263, 245, 246°) for CT, OP, CTSW, and OPSW run respectively. The composited vertical cross-section plots of secondary circulation of CTSW and OPSW run (Figs. 13c, d) also perform similar results with CT and OP run (Figs. 11b, d). Because the intensity of CTSW run is obviously degraded in the simulation, the strength of secondary circulation of CTSW is also reduced. Nevertheless, the overall difference between DS and US side is also revealed. The composited differences in vertical velocity and secondary circulation between CTSW and OPSW run (Figs. 13e, f) are also compared to the results between CT and OP run (Figs. 12a, b). The results also reveal that the existence of the topography could lead to contraction of the inner eyewall and further expansion of the outer rainband or convection over the terrain-influenced area.

Based on the above composite analyses of the convection structure and secondary circulation of the five experiments, features of asymmetric convection and secondary circulation are evident in all experiments, which implies that the asymmetric convection and secondary circulation of Nanmadol were not affected by topography of the Philippines's Luzon Island. However, the existence of the topography may slightly contract the inner eyewall and expand the outer convection zone over the mountain area in this case. It should be noted that Nanmadol only passed over the northeastern tip of Luzon and not over the main high-mountain area of the island (cf. Fig. 2), and there is considerably less destruction of Nanmadol's inner-core compared to storms that traditionally pass the Philippines, as shown in previous studies (e.g., Wu et al. 2003, 2009; Chou et al. 2011).

4.2 Without Talas Sensitivity Experiment

The CTNT experiment is conducted to examine whether the Typhoon Talas (2011) to the east of Nanmadol may play an important role in the maintenance of the uniform and robust vertical wind shear. Figure 14 shows the overall result of the CTNT simulation. It can be found without the effect of Talas, the simulated track shows the more poleward pattern as a comparison the track with CT run (Fig. 14a). Thus, reduces the terrain-influenced time with Luzon Island, the intensity during the simulation period is stronger than CT run (Fig. 14b). The intensity difference between CTNT and CT run at 60 h is about 20 hPa. The synoptic vertical shear and simulated maximum reflectivity of CTNT run at 12 and 60 h (Figs. 14c, d) could be compared to the results with CT run (Figs. 5c, d). It can be found that the cyclonic circulation and convection of Talas are successfully removed from the simulation. The circulation of monsoon gyre still could be clearly identified in the simulation. Furthermore, except the location of Nanmadol and the circulation of the Talas, the general synoptic system during the simulation period are the same with the result of CT run. Meanwhile, the asymmetric convection surrounding the inner core of storm is still clear at this two particular time.

However, the synoptic shear contributes to the simulated storm is slightly different. The 24-48-h composited shear magnitude and shear direction for CTNT run are 7.6 m s^{-1} and 240°, while those values for CT run are 8.7 m s^{-1} and 260°. This result indicates the existence of circulation of Talas could slightly strengthen the shear strength and shift the shear direction clockwise. Regarding the asymmetric convection and secondary circulation of CTNT run (Figs. 14e, f), though the shear direction shows 20° difference, the major maximum area of midlevel vertical velocity is still located to the DS side. And, the feature of the asymmetric secondary circulation is still revealed.

Based on this sensitivity experiment of removing the effect of Talas circulation, it clearly demonstrates that the existence of the circulation of Talas doesn't substantially change the monsoon gyre system which surrounds the Nanmadol. The formation of asymmetric secondary circulation of Nanmadol which induced mainly by environmental vertical shear is evident.

4.3 Model-Physics Sensitivity Experiments

In the model-physics sensitivity experiments, the overall environmental flows, horizontal features, and quadrant-averaged results are consistent with results from the CT and OP runs. For track and intensity simulations of the two sensitivity experiments (Figs. 15a, b), CT2 accurately simulates the storm as it passes the northeastern tip of the Luzon Island, even though the translation speeds of simulated storms are much lower than the values reported by JTWC. In this respect, the storm is not influenced by the topography of Taiwan, and thus its intensity slowly weakens. The simulated intensity at the end of the simulation was 931 hPa, which is nowhere near the observed and CT simulation values (Fig. 3). Therefore, a main analysis of the model simulation is conducted using the CT run, while CT2 is selected for the sensitivity experiments in this study. The track simulations for OP2 run is consistent with those of the OP run; in addition, rightward (cross-track) bias and non-landfalling

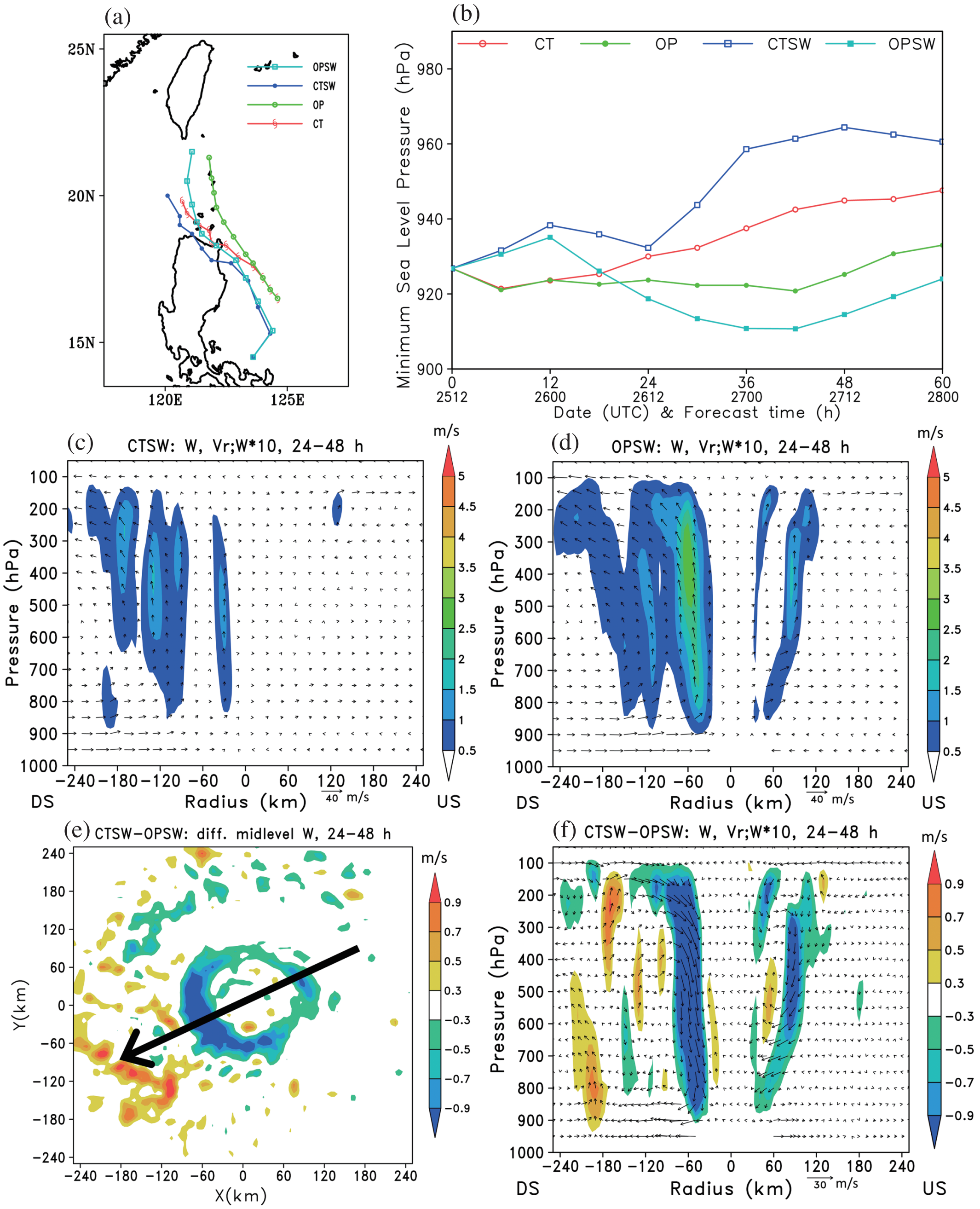

Fig. 13. Simulation results of CTSW and OPSW sensitivity experiments. (a), (b) same as Fig. 3; (c), (d) same as Fig. 11b; and (e), (f) same as Fig. 12. Black vector denotes the 24-48-h time-averaged vertical wind shear direction (245°) calculated from the 10-km grid domain of the CTSW run.

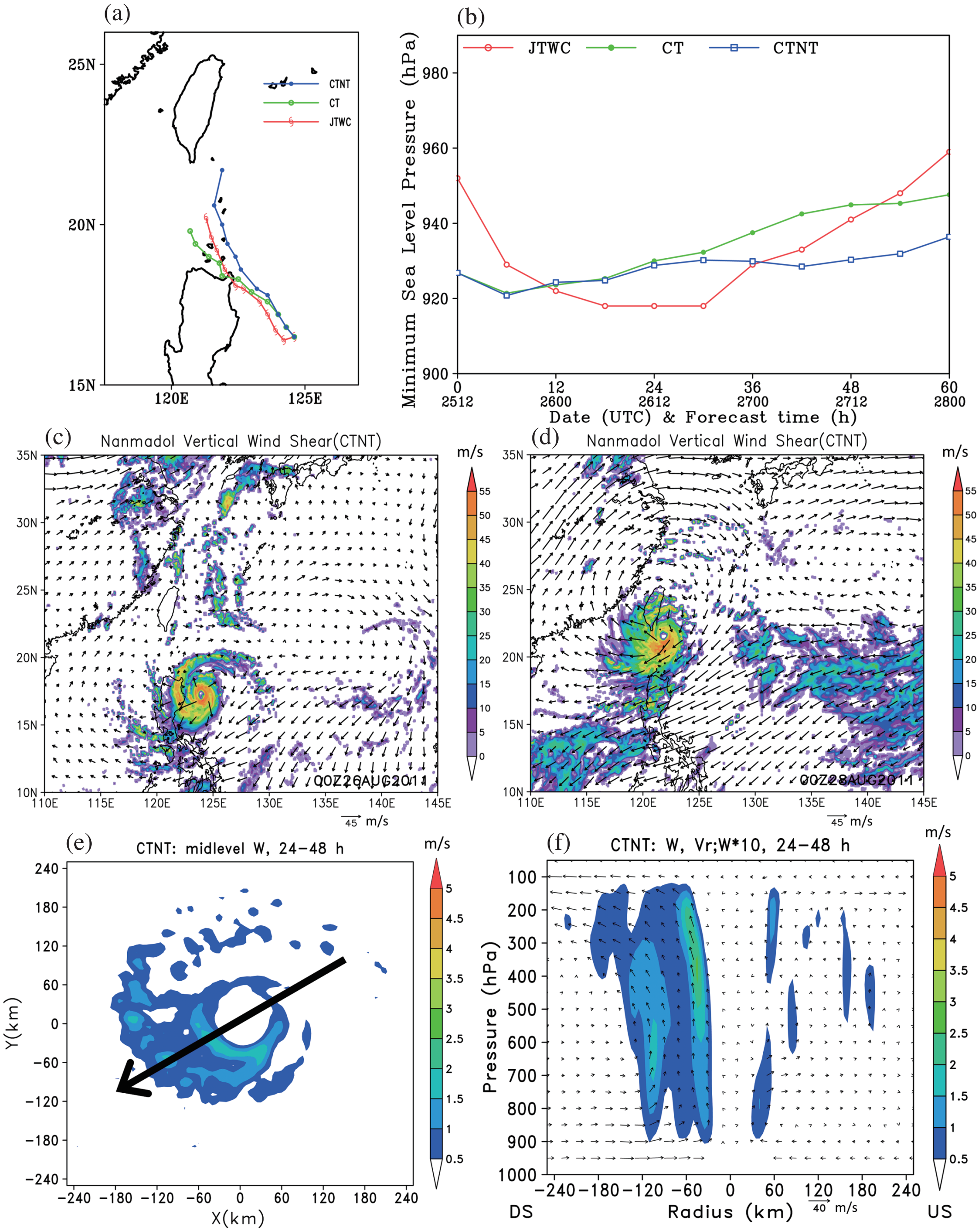

Fig. 14. Simulation results of CTNT sensitivity experiment. (a), (b) same as Fig. 3; (c), (d) same as Figs. 5c, d; and (e), (f) same as Figs. 11a, b. Black vector denotes the 24-48-h time-averaged vertical wind shear direction (240°) calculated from the 10-km grid domain of the CTNT run.

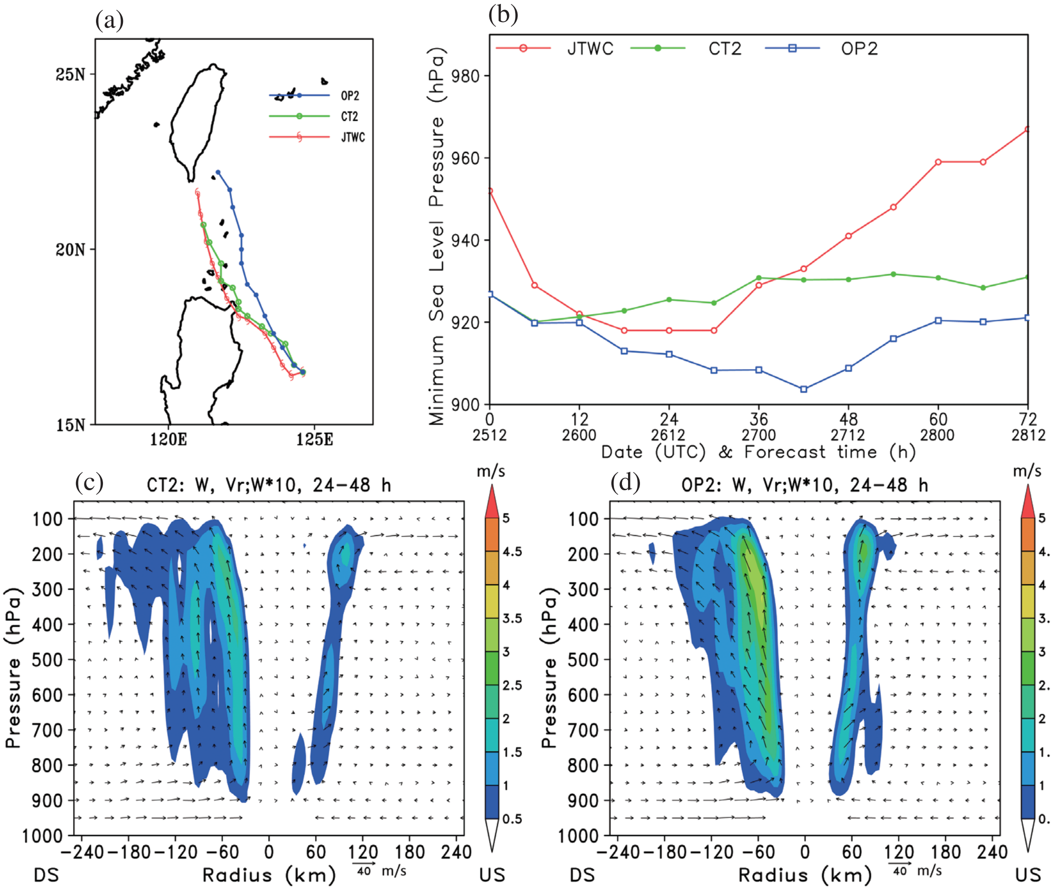

Fig. 15. Simulation results of CT2 and OP2 sensitivity experiments. (a), (b) same as Fig. 3 and (c), (d) same as Fig. 11b.

tracks occurring during the simulation period is also shown in the simulation. However, slight differences are apparent in the OP2 run, where the storm weakens during 12-24 h and results in a larger outer rainband being activated in the simulation (figures not shown).

Based on the model-physics sensitivity experiments, the use of different model physics configurations altered the storm's track and intensity within simulations. This result is consistent with those of recent studies (e.g., Fovell et al. 2009, 2016). Previous literature has shown that different model-physics can cause varying thermodynamic and dynamic influences within the inner-core of the storm, which thus induces different track and intensity results in the model. However, as the main aim of this study is to investigate the convection asymmetry of Nanmadol, a detailed examination of the reason why the use of different model physics in simulations results in varying track and intensity simulations is not addressed in depth.

Figures 15c and d show the 24-48-h averaged vertical cross-section along the shear direction of vertical velocity, and the secondary circulation wind vector for CT2 and OP2 model-physics sensitivity experiments. The shear-induced secondary circulation asymmetries occurring during the storm's interaction with Luzon Island are clearly revealed, with or without the impact of topography. Stronger secondary circulations (deep and strong low-level inflow and upper-level outflow, and strong vertical motion) are clearly seen over the DS side, whereas weaker secondary circulations (thin and weak low-level inflow and upper-level outflow, and weak vertical motion) are seen over the US side. These results clearly demonstrate that the secondary circulation asymmetry of numerical simulations is not overturned by the physics configuration of the model, which implies that this asymmetric feature is driven by actual atmospheric flows, i.e., the environmental vertical wind shear.

5. DISCUSSION

In previous studies (Jones 1995; Wang and Holland 1996; Frank and Ritchie 1999), vortex tilting has been considered the dominant factor explaining formation of the strong vertical updraft over the downshear side. Therefore, vortex tilting of the simulated storms is further examined using most of the experiments (as shown in Fig. 16). The tilting distance is measured from the displacement between 200- and 850-hPa circulation centers, which are defined from the 3.3-km resolution of the third domain. As the tilting distance in the FP run is similar to that of the OP run, the FP result is not discussed here. During most of the simulation time in all of the experiments, the upper circulation center is found to be located in the downshear direction of the lower circulation center. The tilting distances are roughly under 20 km in all cases, and the largest tilting distances are about 40 km during the final part of the simulation in both the CT and OP runs. The average tilting distances are 9.4, 14.0, 5.4, and 8.6 km for CT, OP, CT2, and OP2 respectively. These tilting directions and tilting distances are similar to those obtained from composited radar observations by Reasor et al. (2013), who found that the tilting direction between the 7- and 2-km vortex centers is toward the downshear direction, and that the largest and averaged tilting distances are about 10 and 3 km, respectively, for 52 stochastic nature cases (their Fig. 6).

The tilting distance is also seen to be generally very small, particularly before 48 h. The centers of the upper level and lower level circulations are almost collocated, as shown in the 27-h simulation of the CT run and the 24-h simulation of the OP2 run (Figs. 16a, d); at these particular times, the storm's asymmetric convection and secondary circulation could still be seen in the simulations. Thus, it seems like that the tilting mechanism could not be applied to discuss the appearance of the long-duration and steady-state wavenumber-1 asymmetric convection of Nanmadol. Furthermore, Xu and Wang (2013) argued that Jones (1995)'s vortex tilting and balanced dynamics mechanisms did not work properly in their simulations. They found that the tilting is small and the phase relationship between the asymmetric vertical motion and the temperature anomaly is different from the pattern from the dry dynamics. Their analyses showed that the quasi-balanced vertical motion can only explain a small portion of the simulated asymmetric vertical motions, suggesting that the unbalanced processes must play important roles in the initial development of asymmetric vertical motion and horizontal relative flow.

Recently, Zhang et al. (2013) found that the asymmetric convection pattern may be linked to thermodynamic

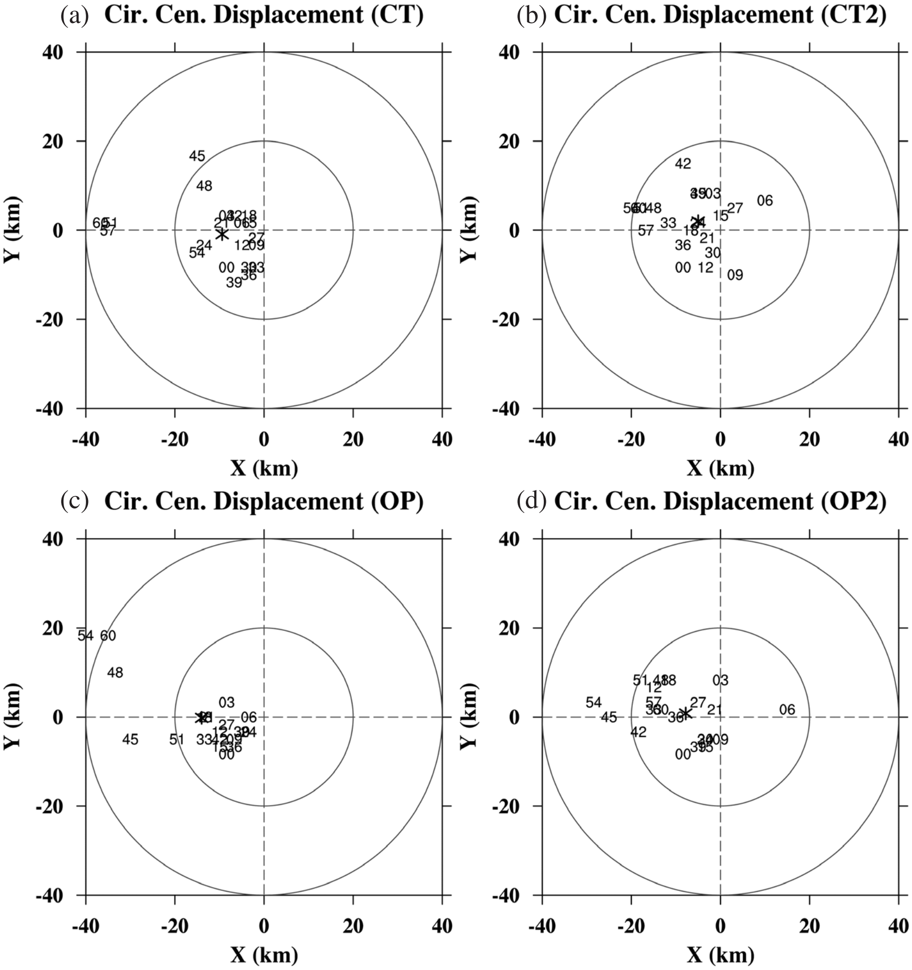

Fig. 16. The center displacement between the 200- and 800-hPa circulation centers for different sensitivity experiments. The circle symbol represents the every 3-h displacement during 0 - 60 h simulation, and the star symbol indicates the 60-h averaged displacement. Unit is km. (a) CT; (b) CT2; (c) OP; and (d) OP2 run.

asymmetry of the boundary layer. They proposed that air parcels obtain heat and moisture from surface fluxes from UL and UR quadrants and that convection is triggered in the DR quadrant when an equivalent potential temperature reaches a maximum value. Convective downdrafts transport cool and dry air to the surface and lower the value of the equivalent potential temperature in the DL and UL quadrants; this cycling process may be directly tied to the shear-induced asymmetry of convection in storms. Hereafter, the thermodynamic patterns are examined in the CT, OP, CT2, and OP2 runs, as shown in Fig. 17. For CT and CT2 experiments (Figs. 17a, c, and e), the higher surface equivalent potential temperature was located in the UR and DR quadrants, while the lower surface equivalent potential temperature appeared in the DL and UL quadrants. The lowest surface equivalent potential temperature was located on the DL side, due to the low surface temperature of Luzon Island's landmass. For the OP and OP2 experiments (Figs. 17b, d, and f), although the differences in the various quadrants were smaller, the higher equivalent potential temperature was still found in the DR and UR quadrants, and the lower equivalent potential temperature was shown in the DL and UL quadrants. Furthermore, the quadrant-averaged profiles of OP and OP2 runs, as well as the CT and CT2, were almost identical, which implies once again that simulation of the surface equivalent potential temperature is not sensitive to the model physics in this study. Based on results from the OP and OP2 runs, the thermodynamic patterns for the different shear-relative quadrants are generally consistent with the results from Zhang et al. (2013), and the region of higher equivalent potential temperature is located on the right of the shear direction. However, when this result is linked to that of vertical motion and convection, the larger asymmetric equivalent potential temperature pattern did not lead to greater asymmetric vertical motion in the CT and CT2 runs. Nevertheless, asymmetric secondary circulations in CT, OP, CT2, and OP2 runs were almost same (Figs. 11b, d, and 15c, d). In this respect, it is considered that if the asymmetry of the surface equivalent potential temperature played a dominant role in triggering the asymmetric vertical motion, then the asymmetric secondary circulation pattern would have been more significant in the CT and CT2 runs.

The above vortex tilting and surface equivalent potential temperature analyses from model simulations show that these two mechanisms are not sufficient to explain the formation of asymmetric vertical motion and convection within storms embedded in a vertical shear environment. Therefore, it is proposed that the superposition effect from the environmental synoptic flow is more important with respect to the formation of convection asymmetry. Figure 18 shows a schematic diagram based on results of asymmetric secondary circulation of the simulated storms (i.e., Figs. 8, 11, and 13). Note that the upper and lower environmental flows could be revealed from the analyses of the non-axisymmetric winds (i.e., Fig. 7e). The convective asymmetry induced by the vertical wind shear can be explained with respect to superposition of the environmental flow and the storm's secondary circulation. For a storm embedded in a typical vertical wind shear condition environment (Fig. 18a), the environmental shear enhances (suppresses) the TC secondary circulation over the downshear (upshear) side, and thus creates an asymmetry of the storm's secondary circulation. The enhanced vertical motion over the downshear side causes the generation of more convection and precipitation, which is then advected by the storm cyclonic circulation to the downshear-left of the storm. Meanwhile, regarding a storm embedded in environmental shear and influenced by the topography as the studied case of Nanmadol (Fig. 18b), vertical shear still dominates the overall convective asymmetry and asymmetric secondary circulation of the simulated storm. However, the topography effect could reduce the storm's primary and secondary circulation, induce extra topographic lifting over the outer area of storm, and cause the contraction of the eyewall.

It is noted here that the dynamic features of asymmetric secondary circulation within a shear influenced storm have been discussed in past studies (Bender 1997; Wong and Chan 2004; Braun et al. 2006; Xu and Wang 2013). However, the analyses in these studies focused on the relative flow and its contribution to lower and upper level convergence (divergence), upward motion and precipitation, and were not directly linked to the storm's secondary circulation, which is highlighted in this study. Bender (1997) showed that when a storm is embedded in an easterly vertical shear, the strong relative wind of the inflow (outflow) is found in the lower free atmosphere (upper layer aloft) over the downshear side. As a result, the upward motion is significantly increased on the downshear side of the storm and reduced on the upshear side, and the precipitation maximum shifts to the downshear-left quadrant. Wong and Chan (2004) proposed a similar schematic diagram (their Fig. 12) to illustrate the difference of the base-state secondary circulation (rising) of the TC in strong and weak shear. However, no more detailed analysis regarding lower and upper relative flows which directly link to secondary circulation could be found. Furthermore, Braun et al. (2006) evaluated several mechanisms for shear-induced azimuthal wavenumber-1 asymmetry. In their case study, it was shown that the relative asymmetric flow of inflow and convergence generally occurs on the downshear side of the eyewall within the lower troposphere but on the upshear side in the upper troposphere. In addition, outflow and divergence were shown to occur on opposite sides in each layer. More recently, based on idealized model simulations, Xu and Wang (2013) proposed a conceptual model for initial development of asymmetric vertical motion in a TC forced by vertical wind shear. When a mature TC confronts environmental flow, the eyewall of the storm plays the role of a material

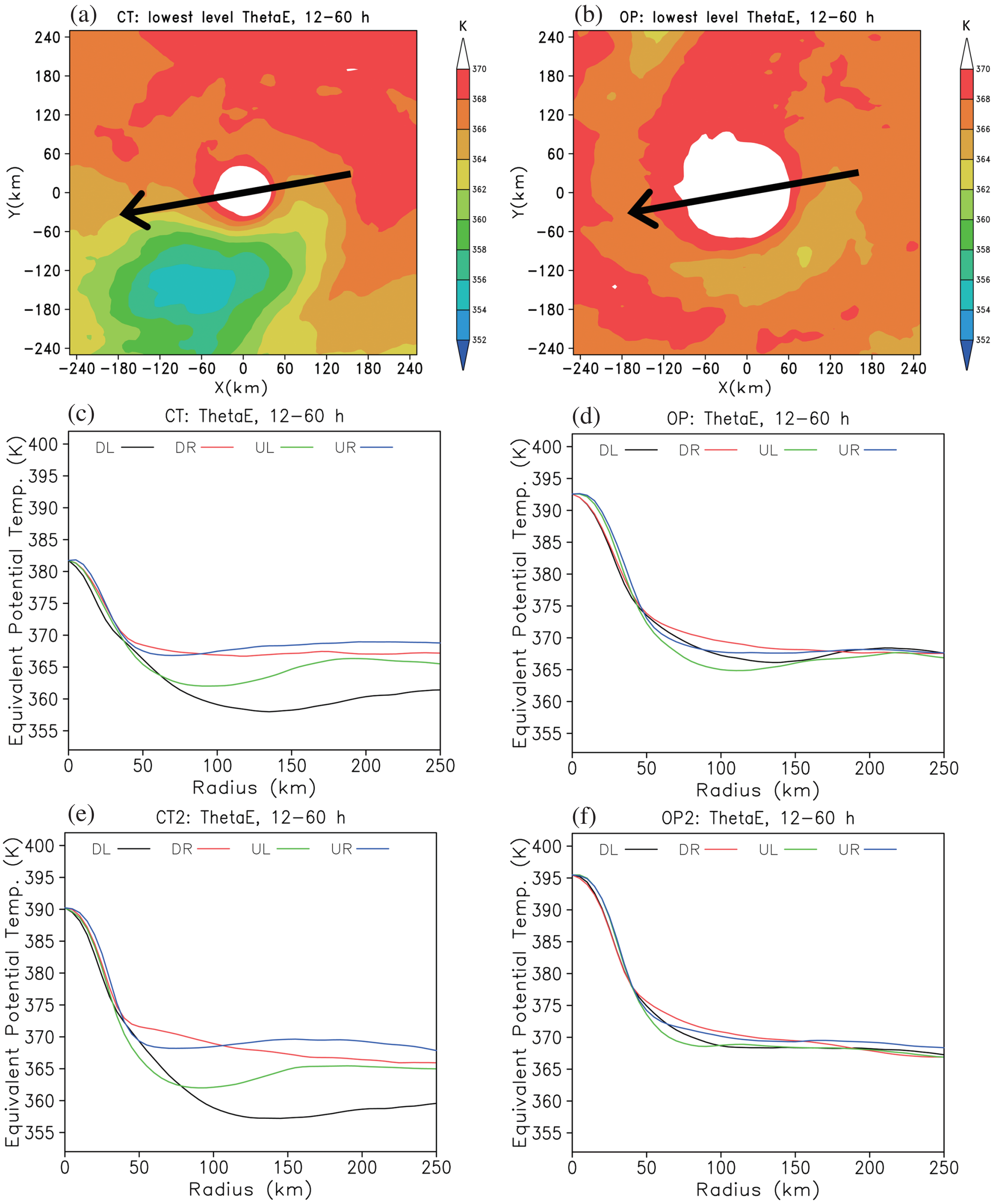

Fig. 17. The 12 - 60 h time-averaged equivalent potential temperature at the lowest model level (σ = 0.997). (a), (b) horizontal distribution of CT and OP run; (c) - (f) the quadrant averaged distribution as function of radius for CT, OP, CT2, and OP2 run respectively. Black vector denotes the 0 - 60 h time-averaged vertical wind shear direction (260°) calculated from the 10-km grid domain of the CT run.

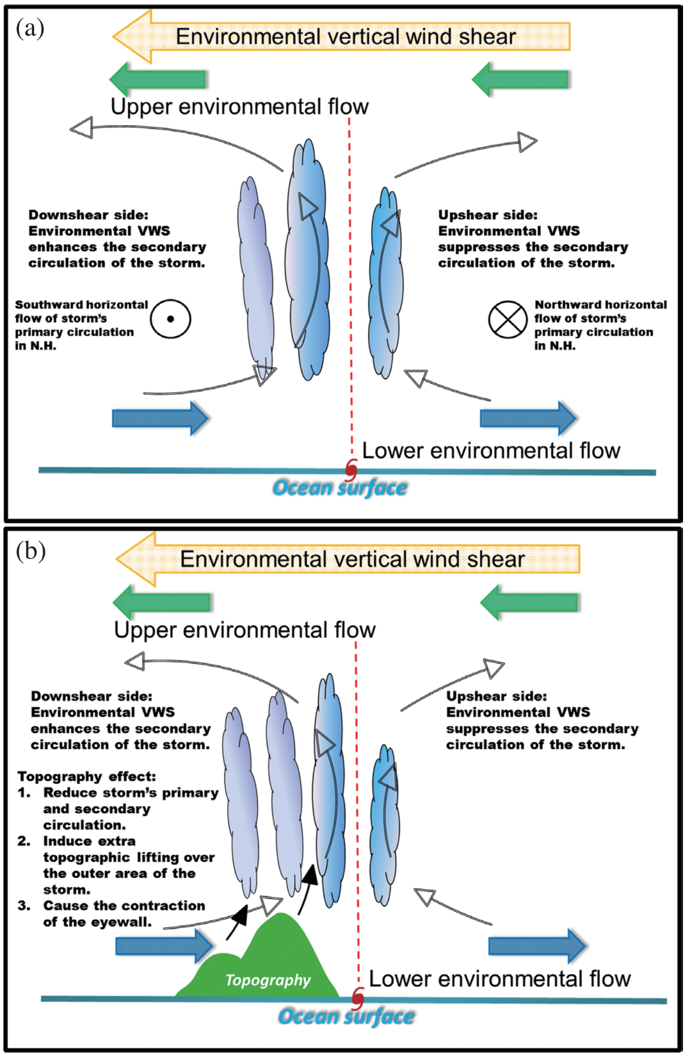

Fig. 18. Conceptual model of formation of convective asymmetry of tropical cyclone. (a) For storm embedded in environmental vertical wind shear; (b) for storm embedded in environmental shear and influenced by the topography. Green and blue arrows denote the environmental upper flow and lower flow respectively. Black open arrows indicate the secondary circulation of the storm. The environmental vertical shear enhances (suppresses) the TC secondary circulation over the downshear (upshear) side, and thus creates the asymmetry of the storm's secondary circulation. The enhanced vertical motions over the downshear side lead to the generation of more convections and precipitation, which is then advected by the storm cyclonic circulation to the downshear-left of the storm.

wall, and the environmental flow induces horizontal convergence in the eyewall upshear and horizontal divergence in the eyewall downshear; horizontal convergence/divergence then drives asymmetric vertical motion along the eyewall following mass conservation.

With respect to relative flows induced by vertical shear wind, the main findings of Bender (1997), Braun et al. (2006), and Xu and Wang (2013), have clearly proven that enhancement of the low-level inflow, or convergence and upper-level outflow, or divergence over the downshear side, are the main factors contributing to the formation of asymmetric convection in a storm. However, the reason for growth in the relative flows on the downshear side has not been clarified. The studies of Bender (1997) and Xu and Wang (2013) use an idealized model simulation framework, where the imposed shear forcing occurs at 72-h of simulation time and then gradually decreases during the simulation.

This situation is therefore different from using real-case simulation frameworks, as shown in both this study and that of Braun et al. (2006). In our study, the almost invariant shear existed at least 60 h, and thus shear forcing could be maintained throughout the whole simulation period. This is considered to be the main reason for the clear asymmetric storm-relative flow and updrafts in the composited results of this study. Furthermore, the asymmetric storm-relative flow shown in this study uses 60-h composites, while that of Braun et al. (2006) is only 6-h because their simulation of Hurricane Bonnie (1998) was embedded in a variant shear environment. Zhang et al. (2013) showed that the inflow layer depth is deeper in downshear quadrants and that the downshear right quadrant is the deepest, based on dropsonde and Doppler radar composites (their Fig. 4). Nevertheless, regardless of the differences in model frameworks and composite-time in real cases, the features of asymmetric relative-flows are clearly revealed in these model-basis studies and in recent observational results. However, as previously mentioned, the reasons for linking the formation of relative-flow and its method to vertical updraft are not well addressed.

Hereafter in this study, the proposed superposition effect from the basic flow to the storm's secondary circulation is used to explain formation of the asymmetric relative flows (i.e., low-level inflow and upper-level outflow) and the middle updraft, where revealed in the strong shear environment.

6. CONCLUSION

The intensity and structure of Typhoon Nanmadol (2011) were affected by the land mass when it passed Luzon Island. Furthermore, Nanmadol was also embedded within a high vertical wind shear environment during this period, which induced obvious asymmetric convection around the storm. In this study, the Weather Research and Forecasting model was applied using the finest resolution of 3.3 km to conduct numerical experiments, with the aim of understanding the effects of terrain and environmental vertical wind shear on the intensity, structure and asymmetric convection of Nanmadol as it passed Luzon Island. Terrain-removed sensitivity experiments were also conducted to elucidate the relative role of flow-blocking by the terrain and the friction effect of the landscape with respect to formation of the storm's asymmetric convection. In addition, the effect of the adjacent weather system Typhoon Talas (2011) was investigated. Furthermore, model-physics sensitivity experiments using different cloud microphysics schemes were conducted to examine whether the asymmetric convective structures of the simulated storm were influenced by the model physics.

Based on the simulated result from the CT run, the overall track and intensity evolution of Nanmadol were reasonably simulated, although there were small differences in the timing of its landfall on Luzon Island and a much smaller translation speed of the simulated storm. In particular, the model was able to simulate the storm passing the northeastern tip of Luzon Island and could simulate its associated decrease in intensity due to topography. The model also performed well in capturing the active downshear-left convection relative to the storm center, with respect to the simulation of asymmetric convection; this asymmetric convection was consistent with the observed satellite microwave images. Further analyses indicate that convection was originally enhanced over the downshear side, and it then advected to the left of the vertical shear direction due to the cyclonic circulation of the storm. Moreover, based on a relative flow and vertical motion analysis of the storm, results show that the thickness and strength of the low-level inflow and upper-level outflow, as well as the width and strength of the midlevel vertical velocity, were stronger over the downshear side than those over the upshear side. This result implies that vertical wind shear led to the formation of this storm's asymmetric secondary circulation.

The results from two topography-removed and two different vortex-implanted location sensitivity experiments provide no obvious link between asymmetric convection and secondary circulation and the topography of Luzon Island, although the existence of terrain could lead to contraction of the inner eyewall and to the active outer spiral rainband over the high mountain areas (downshear side in this study case). This result indicates that the environmental vertical wind shear played a dominant role in formation of the asymmetric convection of Nanmadol. With respect to sensitivity experiments using different model physics, the shear-induced secondary circulation asymmetries were successfully revealed in model-physics sensitivity experiments: the stronger secondary circulations were clearly revealed over the downshear side, while the weaker secondary circulations were found over the upshear side. Although several previous studies have reported that different model-physics can induce different storm structures, the results of this study clearly demonstrate that the secondary circulation asymmetry of the numerical simulations conducted were not influenced by the physics configuration of the model. The sensitivity experiments conducted here not only indicated that environmental vertical wind shear played a dominant role in forming the asymmetric convective pattern of Nanmadol, but also demonstrated that the proposed shear-induced dynamic pattern of asymmetric secondary circulation was robust and not sensitive to different configurations of model physics.

To explain why asymmetric convection and secondary circulation formed in the simulated storm, we examined the vortex tilting distance and surface equivalent potential temperature distribution. The results showed that the tilting distances were very small and the storm centers are vertically collocated at some simulation time. However, the analysis shows a larger asymmetric surface equivalent potential temperature in the CT run compared to the OP run, although there were little differences in the asymmetric convection and secondary circulation between the control and OP runs. Based on these results, it is speculated that the mechanisms of vortex tilting (Jones 1995) and the intrusion of high surface enthalpy fluxes (Zhang et al. 2013) are insufficient to explain the formation of asymmetric vertical motion and convection for storms embedded in the vertical shear environment. This study proposes the importance of the superposition effect of environmental flows on the storm's secondary circulation in the formation of convection asymmetry. The environmental shear flows enhance (suppress) the TC secondary circulation over the downshear (upshear) side, and thus create an asymmetry of the storm's secondary circulation. The enhanced vertical motions over the downshear side lead to the generation of a greater amount of convection and precipitation, which is then advected by the storm's cyclonic circulation to the downshear-left of the storm. The dynamic features of the asymmetric secondary circulation for a shear influenced storm has already been addressed in previous studies (Bender 1997; Wong and Chan 2004; Braun et al. 2006; Xu and Wang 2013), but the analyses of such studies focused on the relative flow and its contribution to the lower and upper level convergence (divergence), upward motion and precipitation, and did not make a direct link to the enhancement or suppression of the storm's secondary circulation, which is dynamically related to vertical wind shear, as determined and highlighted in this study.

However, the shear magnitudes obtained from the current model simulations were over-estimated in this study and may have dominated the results with respect to the relationship between shear and land interactions and the evolution of convection asymmetries. Therefore, to examine this uncertainty, the same study approach has been applied to Typhoon Kalmaegi (2014), which was also embedded in a nearly invariant high northeasterly shear environment when it passed the Philippines. The more accurate evolution of TC's intensity and environment vertical shear could be simulated, and the overall results of the formations of the asymmetric secondary circulation and convection are consistent with the finding in this study (figures not shown). In addition, ongoing works aim to examine the proposed conceptual model using storms influenced by different environmental shear patterns, and in this respect, we aim to discover the formation of shear-induced asymmetric secondary circulation in other tropical storms occurring in different seasons and basins. It is anticipated that this dynamical pattern could be used to explain the formation of asymmetric tropical cyclone convection (for example, Figure-6 and Figure-9 convection embedded in northerly and southerly vertical shear, respectively), and that the asymmetric secondary circulation pattern could also be found within storms embedded in different shear patterns, based on several real-case storm simulations (details not shown in this manuscript). Furthermore, it is suggested that the dynamic features of secondary circulation, in particular the upper-level flow, could be examined using composite analyses of aircraft-deployed dropsondes, or satellite atmospheric motion vector observations, to obtain convincing results that support the conceptual model proposed in this study (e.g., Uhlhorn et al. 2014; Oyama 2017). Although a detailed examination of the mechanisms related to vorticity conservation and budget analysis (e.g., Bender 1997; Braun et al. 2006) and eyewall convergence changes with height (Xu and Wang 2013) were not visited in the current analyses, it is anticipated that these issues will be addressed and related to secondary circulation in future studies.

Acknowledgements The work is supported by the National Science Council of Taiwan through Grants MOST 107-2111-M-034-004 and MOST 107-2119-M-002-053. The authors also want to thank three anonymous reviewers and the editor for thorough reviews that helped improve the clarity of the manuscript. This manuscript was edited by Wallace Academic Editing. The TC best track data were JTWC (http://www.usno.navy.mil/JTWC/best-track-archive); the microwave images were provided from the Naval Research Laboratory, Monterey, California (http://www.nrlmry.navy.mil/TC.html); the NCEP FNL operational model global tropospheric analyses were obtained from NCEP/NWS/NOAA (http://rda.ucar.edu).

REFERENCES

Bender, M. A., 1997: The effect of relative flow on the asymmetric structure in the interior of hurricanes. *J. Atmos. Sci.*, **54**, 703-724, doi: 10.1175/1520-0469(1997)054<0703:TEORFO>2.0.CO;2. [Link]

Bender, M. A., R. E. Tuleya, and Y. Kurihara, 1987: A Numerical Study of the Effect of Island Terrain on Tropical Cyclones. *Mon. Weather Rev.*, **115**, 130-155, doi: 10.1175/1520-0493(1987)115<0130:ANSOTE>2.0.CO;2. [Link]

Black, M. L., J. F. Gamache, F. D. Marks, C. E. Samsury, and H. E. Willoughby, 2002: Eastern Pacific Hurricanes Jimena of 1991 and Olivia of 1994: The effect of vertical shear on structure and intensity. *Mon. Weather Rev.*, **130**, 2291-2312, doi: 10.1175/1520-0493(2002)130<2291:EPHJOA>2.0.CO;2. [Link]

Brand, S. and J. W. Blelloch, 1973: Changes in the Characteristics of Typhoons Crossing the Philippines. *J. Appl. Meteorol.*, **12**, 104-109, doi: 10.1175/1520-0450(1973)012<0104:CITCOT>2.0.CO;2. [Link]

Braun, S. A., M. T. Montgomery, and Z. Pu, 2006: High-resolution simulation of Hurricane Bonnie (1998). Part I: The organization of eyewall vertical motion. *J. Atmos. Sci.*, **63**, 19-42, doi: 10.1175/JAS3598.1. [Link]

Braun, S. A., J. A. Sippel, and D. S. Nolan, 2012: The impact of dry midlevel air on hurricane intensity in idealized simulations with no mean flow. *J. Atmos. Sci.*, **69**, 236-257, doi: 10.1175/JAS-D-10-05007.1. [Link]

Chih, C.-H., K.-H. Chou, and S. Chiao, 2015: Topography and tropical cyclone structure influence on eyewall evolution in Typhoon Sinlaku (2008). *Terr. Atmos. Ocean. Sci.*, **26**, 571-586, doi: 10.3319/TAO.2015.05.08.01(A). [Link]

Chou, K.-H. and C.-C. Wu, 2008: Typhoon initialization in a mesoscale model—Combination of the bogused vortex and the dropwindsonde data in DOTSTAR. *Mon. Weather Rev.*, **136**, 865-879, doi: 10.1175/2007MWR2141.1. [Link]

Chou, K.-H., C.-C. Wu, and Y. Wang, 2011: Eyewall evolution of typhoons crossing the Philippines and Taiwan: An observational study. *Terr. Atmos. Ocean. Sci.*, **22**, 535-548, doi: 10.3319/TAO.2011.05.10.01(TM). [Link]

Corbosiero, K. L. and J. Molinari, 2002: The effects of vertical wind shear on the distribution of convection in tropical cyclones. *Mon. Weather Rev.*, **130**, 2110-2123, doi: 10.1175/1520-0493(2002)130<2110:TEOVWS>2.0.CO;2. [Link]

Corbosiero, K. L. and J. Molinari, 2003: The relationship between storm motion, vertical wind shear, and convective asymmetries in tropical cyclones. *J. Atmos. Sci.*, **60**, 366-376, doi: 10.1175/1520-0469(2003)060<0366:TRBSMV>2.0.CO;2. [Link]

DeHart, J. C., R. A. Houze, and R. F. Rogers, 2014: Quadrant distribution of tropical cyclone inner-core kinematics in relation to environmental shear. *J. Atmos. Sci.*, **71**, 2713-2732, doi: 10.1175/JAS-D-13-0298.1. [Link]

DeMaria, M., 1996: The effect of vertical shear on tropical cyclone intensity change. *J. Atmos. Sci.*, **53**, 2076-2088, doi: 10.1175/1520-0469(1996)053<2076:TEOVSO>2.0.CO;2. [Link]

Dudhia, J., 1989: Numerical study of convection observed during the winter monsoon experiment using a mesoscale two-dimensional model. *J. Atmos. Sci.*, **46**, 3077-3107, doi: 10.1175/1520-0469(1989)046<3077:NSOCOD>2.0.CO;2. [Link]

Fovell, R. G., K. L. Corbosiero, and H.-C. Kuo, 2009: Cloud microphysics impact on hurricane track as revealed in idealized experiments. *J. Atmos. Sci.*, **66**, 1764-1778, doi: 10.1175/2008JAS2874.1. [Link]

Fovell, R. G., Y. Bu, K. L. Corbosiero, W. Tung, Y. Cao, H. Kuo, L. Hsu, and H. Su, 2016: Influence of Cloud Microphysics and Radiation on Tropical Cyclone Structure and Motion. *Meteorol. Monogr.*, **56**, 11.1-11.27, doi: 10.1175/AMSMONOGRAPHS-D-15-0006.1. [Link]

Frank, W. M. and E. A. Ritchie, 1999: Effects of environmental flow upon tropical cyclone structure. *Mon. Weather Rev.*, **127**, 2044-2061, doi: 10.1175/1520-0493(1999)127<2044:EOEFUT>2.0.CO;2. [Link]

Frank, W. M. and E. A. Ritchie, 2001: Effects of vertical wind shear on the intensity and structure of numerically simulated hurricanes. *Mon. Weather Rev.*, **129**, 2249-2269, doi: 10.1175/1520-0493(2001)129<2249:EOVWSO>2.0.CO;2. [Link]

Grell, G. A. and D. Dévényi, 2002: A generalized approach to parameterizing convection combining ensemble and data assimilation techniques. *Geophys. Res. Lett.*, **29**, 38-1-38-4, doi: 10.1029/2002GL015311. [Link]

Hence, D. A. and R. A. Houze, 2011: Vertical structure of hurricane eyewalls as seen by the TRMM Precipitation Radar. *J. Atmos. Sci.*, **68**, 1637-1652, doi: 10.1175/2011JAS3578.1. [Link]

Hsu, L.-H., H.-C. Kuo, and R. G. Fovell, 2013: On the geographic asymmetry of typhoon translation speed across the mountainous island of Taiwan. *J. Atmos. Sci.*, **70**, 1006-1022, doi: 10.1175/jas-d-12-0173.1. [Link]

Huang, Y.-H., C.-C. Wu, and Y. Wang, 2011: The influence of island topography on typhoon track deflection. *Mon. Weather Rev.*, **139**, 1708-1727, doi: 10.1175/2011mwr3560.1. [Link]

Jian, G.-J. and C.-C. Wu, 2008: A numerical study of the track deflection of Supertyphoon Haitang (2005) prior to its landfall in Taiwan. *Mon. Weather Rev.*, **136**, 598-615, doi: 10.1175/2007MWR2134.1. [Link]

Jones, S. C., 1995: The evolution of vortices in vertical shear. I: Initially barotropic vortices. *Q. J. R. Meteorol. Soc.*, **121**, 821-851, doi: 10.1002/qj.49712152406. [Link]

Knaff, J. A., C. R. Sampson, and M. DeMaria, 2005: An operational Statistical Typhoon Intensity Prediction Scheme for the western North Pacific. *Weather Forecast.*, **20**, 688-699, doi: 10.1175/WAF863.1. [Link]

Lim, J.-O. J. and S.-Y. Hong, 2005: Effects of bulk ice microphysics on the simulated monsoonal precipitation over east Asia. *J. Geophys. Res.*, **110**, D24201, doi: 10.1029/2005JD006166. [Link]

Lin, Y.-L., R. D. Farley, and H. D. Orville, 1983: Bulk parameterization of the snow field in a cloud model. *J. Clim. Appl. Meteorol.*, **22**, 1065-1092, doi: 10.1175/1520-0450(1983)022<1065:BPOTSF>2.0.CO;2. [Link]

Lin, Y.-L., S.-Y. Chen, C. M. Hill, and C.-Y. Huang, 2005: Control parameters for the influence of a mesoscale mountain range on cyclone track continuity and deflection. *J. Atmos. Sci.*, **62**, 1849-1866, doi: 10.1175/JAS3439.1. [Link]

Low-Nam, S. and C. Davis, 2001: Development of a tropical cyclone bogussing scheme for the MM5 system. Preprints, 11th PSU/NCAR Mesoscale Model Users' Workshop, National Center for Atmospheric Research, Boulder, CO, 130-134.

Mlawer, E. J., S. J. Taubman, P. D. Brown, M. J. Iacono, and S. A. Clough, 1997: Radiative transfer for inhomogeneous atmospheres: RRTM, a validated correlated-k model for the longwave. *J. Geophys. Res.*, **102**, 16663-16682, doi: 10.1029/97JD00237. [Link]

Molinari, J., J. Frank, and D. Vollaro, 2013: Convective bursts, downdraft cooling, and boundary layer recovery in a sheared tropical storm. *Mon. Weather Rev.*, **141**, 1048-1060, doi: 10.1175/MWR-D-12-00135.1. [Link]

Montgomery, M. T. and R. J. Kallenbach, 1997: A theory for vortex rossby-waves and its application to spiral bands and intensity changes in hurricanes. *Q. J. R. Meteorol. Soc.*, **123**, 435-465, doi: 10.1002/qj.49712353810. [Link]

Oyama, R., 2017: Relationship between Tropical Cyclone Intensification and Cloud-top Outflow Revealed by Upper-Tropospheric Atmospheric Motion Vectors. *J. Appl. Meteorol. Climatol.*, **56**, 2801-2819, doi: 10.1175/jamc-d-17-0058.1. [Link]

Pleim, J. E., 2007: A combined local and nonlocal closure model for the atmospheric boundary layer. Part II: Application and evaluation in a mesoscale meteorological model. *J. Appl. Meteorol. Climatol.*, **46**, 1396-1409, doi: 10.1175/JAM2534.1. [Link]

Powell, M. D., 1982: The transition of the hurricane Frederic boundary-layer wind field from the open Gulf of Mexico to landfall. *Mon. Weather Rev.*, **110**, 1912-1932, doi: 10.1175/1520-0493(1982)110<1912:TTOTHF>2.0.CO;2. [Link]

Powell, M. D., 1987: Changes in the low-level kinematic and thermodynamic structure of hurricane Alicia (1983) at landfall. *Mon. Weather Rev.*, **115**, 75-99, doi: 10.1175/1520-0493(1987)115<0075:CITLLK>2.0.CO;2. [Link]

Reasor, P. D., R. Rogers, and S. Lorsolo, 2013: Environmental flow impacts on tropical cyclone structure diagnosed from airborne Doppler radar composites. *Mon. Weather Rev.*, **141**, 2949-2969, doi: 10.1175/MWR-D-12-00334.1. [Link]

Riemer, M., M. T. Montgomery, and M. E. Nicholls, 2010: A new paradigm for intensity modification of tropical cyclones: Thermodynamic impact of vertical wind shear on the inflow layer. *Atmos. Chem. Phys.*, **10**, 3163-3188, doi: 10.5194/acp-10-3163-2010. [Link]

Rodgers, E. B., S. W. Chang, and H. F. Pierce, 1994: A satellite observational and numerical study of precipitation characteristics in western North Atlantic tropical cyclones. *J. Appl. Meteorol.*, **33**, 129-139, doi: 10.1175/1520-0450(1994)033<0129:ASOANS>2.0.CO;2. [Link]

Rogers, R. F., P. Reasor, and S. Lorsolo, 2013: Airborne Doppler observations of the inner-core structural differences between intensifying and steady-state tropical cyclones. *Mon. Weather Rev.*, **141**, 2970-2991, doi: 10.1175/MWR-D-12-00357.1. [Link]

Schubert, W. H., M. T. Montgomery, R. K. Taft, T. A. Guinn, S. R. Fulton, J. P. Kossin, and J. P. Edwards, 1999: Polygonal eyewalls, asymmetric eye contraction, and potential vorticity mixing in hurricanes. *J. Atmos. Sci.*, **56**, 1197-1223, doi: 10.1175/1520-0469(1999)056<1197:PEAECA>2.0.CO;2. [Link]

Shapiro, L. J., 1983: The asymmetric boundary layer flow under a translating hurricane. *J. Atmos. Sci.*, **40**, 1984-1998, doi: 10.1175/1520-0469(1983)040<1984:TABLFU>2.0.CO;2. [Link]

Skamarock, W. C., J. B. Klemp, J. Dudhia, D. O. Gill, D. M. Barker, M. G. Duda, X.-Y. Huang, W. Wang, and J. G. Powers, 2008: A description of the Advanced Research WRF version 3. NCAR Technical Note NCAR/TN-475+STR, Mesoscale and Microscale Meteorology Division, National Center for Atmospheric Research, Boulder, Colorado, USA, 113 pp, doi: 10.5065/D68S4MVH. [Link]

Smith, R. K. and G. L. Thomsen, 2010: Dependence of tropical-cyclone intensification on the boundary-layer representation in a numerical model. *Q. J. R. Meteorol. Soc.*, **136**, 1671-1685, doi: 10.1002/qj.687. [Link]

Tang, B. and K. Emanuel, 2010: Midlevel ventilation's constraint on tropical cyclone intensity. *J. Atmos. Sci.*, **67**, 1817-1830, doi: 10.1175/2010JAS3318.1. [Link]

Tang, B. and K. Emanuel, 2012: Sensitivity of tropical cyclone intensity to ventilation in an axisymmetric model. *J. Atmos. Sci.*, **69**, 2394-2413, doi: 10.1175/JAS-D-11-0232.1. [Link]

Tang, C. K. and J. C. L. Chan, 2015: Idealized simulations of the effect of local and remote topographies on tropical cyclone tracks. *Q. J. R. Meteorol. Soc.*, **141**, 2045-2056, doi: 10.1002/qj.2498. [Link]

Tuleya, R. E., 1994: Tropical storm development and decay: Sensitivity to surface boundary conditions. *Mon. Weather Rev.*, **122**, 291-304, doi: 10.1175/1520-0493(1994)122<0291:TSDADS>2.0.CO;2. [Link]

Uhlhorn, E. W., B. W. Klotz, T. Vukicevic, P. D. Reasor, and R. F. Rogers, 2014: Observed hurricane wind speed asymmetries and relationships to motion and environmental shear. *Mon. Weather Rev.*, **142**, 1290-1311, doi: 10.1175/MWR-D-13-00249.1. [Link]

Wang, C.-C., H.-C. Kuo, Y.-H. Chen, H.-L. Huang, C.-H. Chung, and K. Tsuboki, 2012: Effects of asymmetric latent heating on typhoon movement crossing Taiwan: The case of Morakot (2009) with extreme rainfall. *J. Atmos. Sci.*, **69**, 3172-3196, doi: 10.1175/JAS-D-11-0346.1. [Link]

Wang, Y. and G. J. Holland, 1996: Tropical cyclone motion and evolution in vertical shear. *J. Atmos. Sci.*, **53**, 3313-3332, doi: 10.1175/1520-0469(1996)053<3313:TCMAEI>2.0.CO;2. [Link]

Wang, Y. and C.-C. Wu, 2004: Current understanding of tropical cyclone structure and intensity changes – A review. *Meteorol. Atmos. Phys.*, **87**, 257-278, doi: 10.1007/s00703-003-0055-6. [Link]

Willoughby, H. E., H.-L. Jin, S. J. Lord, and J. M. Piotrowicz, 1984: Hurricane structure and evolution as simulated by an axisymmetric, nonhydrostatic numerical model. *J. Atmos. Sci.*, **41**, 1169-1186, doi: 10.1175/1520-0469(1984)041<1169:HSAEAS>2.0.CO;2. [Link]

Wingo, M. T. and D. J. Cecil, 2010: Effects of vertical wind shear on tropical cyclone precipitation. *Mon. Weather Rev.*, **138**, 645-662, doi: 10.1175/2009MWR2921.1. [Link]

Wong, M. L. M. and J. C. L. Chan, 2004: Tropical cyclone intensity in vertical wind shear. *J. Atmos. Sci.*, **61**, 1859-1876, doi: 10.1175/1520-0469(2004)061<1859:TCIIVW>2.0.CO;2. [Link]

Wu, C.-C., K.-H. Chou, H.-J. Cheng, and Y. Wang, 2003: Eyewall contraction, breakdown and reformation in a landfalling typhoon. *Geophys. Res. Lett.*, **30**, doi: 10.1029/2003Gl017653. [Link]

Wu, C.-C., H.-J. Cheng, Y. Wang, and K.-H. Chou, 2009: A numerical investigation of the eyewall evolution in a landfalling typhoon. *Mon. Weather Rev.*, **137**, 21-40, doi: 10.1175/2008MWR2516.1. [Link]

Wu, L., S. A. Braun, J. Halverson, and G. Heymsfield, 2006: A numerical study of Hurricane Erin (2001). Part I: Model verification and storm evolution. *J. Atmos. Sci.*, **63**, 65-86, doi: 10.1175/JAS3597.1. [Link]

Xu, Y. and Y. Wang, 2013: On the initial development of asymmetric vertical motion and horizontal relative flow in a mature tropical cyclone embedded in environmental vertical shear. *J. Atmos. Sci.*, **70**, 3471-3491, doi: 10.1175/JAS-D-12-0335.1. [Link]

Yang, M.-J., D. L. Zhang, and H.-L. Huang, 2008: A modeling study of Typhoon Nari (2001) at landfall. Part I: Topographic effects. *J. Atmos. Sci.*, **65**, 3095-3115, doi: 10.1175/2008JAS2453.1. [Link]

Yang, M.-J., D.-L. Zhang, X.-D. Tang, and Y. Zhang, 2011: A modeling study of Typhoon Nari (2001) at landfall: 2. Structural changes and terrain-induced asymmetries. *J. Geophys. Res.*, **116**, D09112, doi: 10.1029/2010JD015445. [Link]

Yeh, T.-C. and R. L. Elsberry, 1993a: Interaction of typhoons with the Taiwan orography. Part I: Upstream track deflections. *Mon. Weather Rev.*, **121**, 3193-3212, doi: 10.1175/1520-0493(1993)121<3193:IOTWTT>2.0.CO;2. [Link]

Yeh, T.-C. and R. L. Elsberry, 1993b: Interaction of typhoons with the Taiwan orography. Part II: Continuous and discontinuous tracks across the island. *Mon. Weather Rev.*, **121**, 3213-3233, doi: 10.1175/1520-0493(1993)121<3213:IOTWTT>2.0.CO;2. [Link]

Yu, C.-K. and L.-W. Cheng, 2013: Distribution and mechanisms of orographic precipitation associated with Typhoon Morakot (2009). *J. Atmos. Sci.*, **70**, 2894-2915, doi: 10.1175/JAS-D-12-0340.1. [Link]

Zhang, J. A., R. F. Rogers, P. D. Reasor, E. W. Uhlhorn, and F. D. Marks, 2013: Asymmetric hurricane boundary layer structure from dropsonde composites in relation to the environmental vertical wind shear. *Mon. Weather Rev.*, **141**, 3968-3984, doi: 10.1175/MWR-D-12-00335.1. [Link]